

AD-A148 686

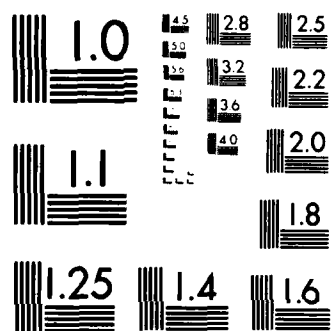
ACOUSTIC TOMOGRAPHY IN BOREHOLES USING AN ALGEBRAIC  
RECONSTRUCTION TECHNIQUE(U) COLORADO SCHOOL OF MINES  
GOLDEN CENTER FOR WAVE PHENOMENA K L SMITH 05 NOV 84  
CWP-012 N00014-84-K-0049 F/G 8/11

1/1

UNCLASSIFIED

F/G 8/11

NL



MICROCOPY RESOLUTION TEST CHART  
NATIONAL BUREAU OF STANDARDS 1963-A

12

CSM



Acoustic Tomography in Boreholes  
using an Algebraic Reconstruction Technique.

by  
Kingsley L. Smith

Partially supported by the Selected Research Opportunities  
Program of the Office of Naval Research

AD-A 148 686

**Colorado School of Mines**  
Golden, Colorado 80401

Center for Wave Phenomena  
Department of Mathematics  
303/273-3557

DTIC FILE COPY

DTIC  
ELECTE  
DEC 17 1984  
S E D

This document has been approved  
for public use and sale; its  
distribution is unlimited.



84 12 06 012



**Acoustic Tomography in Boreholes  
using an Algebraic Reconstruction Technique.**

by  
**Kingsley L. Smith**

**Partially supported by the Selected Research Opportunities  
Program of the Office of Naval Research**

**Center for Wave Phenomena  
Department of Mathematics  
Colorado School of Mines  
Golden, Colorado 80401  
Phone: (303) 273-3557**

**IC  
TE  
1984**

**D**

### ABSTRACT

An algebraic reconstruction technique (ART) is described for the seismic tomography of velocities from the travel times of a multiple offset vertical seismic profile. ART concentrates on the production of a reconstructed field whose projected data (travel times) agree with the observed data. This reconstructed field is modified by altering the data for each ray such that when this data is back-projected, the new image agrees with the original data. Because the paths of the rays must be known to calculate the expected travel times, the problem is linearized by using raypath approximations as determined from either a constant or a linear  $c(z)$  velocity medium.

Imaging of synthetic data revealed that the orientation of the anomaly affects both the rate of convergence and the resolution of the reconstructed field. Some smoothing of the velocity anomalies occurred along the direction of the rays.

Noisy data sets developed problems in the reconstructed velocity field. Huge single point anomalies appeared along the model's edge in the reconstructed image. Elimination of these errant anomalies was necessary to obtain a reasonable velocity reconstruction. Because isotropy was assumed, the algorithm poorly reconstructed data which was collected over the strongly anisotropic Pierre Shale.

## TABLE OF CONTENTS

Abstract . . . . .	i
Table of Contents . . . . .	ii
Notation . . . . .	iii
1. Introduction . . . . .	1
2. Algebraic Reconstruction Technique - ART . . . . .	4
2.1 Constant Background . . . . .	5
2.2 Constant Background - Iterative Algorithm. . . . .	8
2.3 Linear $c(z)$ Medium . . . . .	10
2.4 Linear $c(z)$ Medium - Iterative Algorithm . . . . .	14
3. Testing the Algorithms . . . . .	16
4. Results . . . . .	17
5. Pierre Shale Experiment . . . . .	19
6. Conclusions . . . . .	24
References . . . . .	26
Appendix A: Ray Parameter Derivation . . . . .	28
Appendix B: Travel Time Calculation . . . . .	31

**Accession For**

NRIS GRAB	<input checked="" type="checkbox"/>
DALS TAB	<input type="checkbox"/>
Unsub	<input type="checkbox"/>

From \_\_\_\_\_  
Date \_\_\_\_\_

\_\_\_\_\_ Codes  
\_\_\_\_\_/yr  
\_\_\_\_\_

A-1

# NOTATION

$\alpha$	Angle formed by the length of the raypath.
$c_0$	Velocity at the surface.
$c(z)$	Velocity.
$d^{mn}$	Sum of chord lengths.
$e_{ij}^{mn}$	Residual error time for chord length.
$E_{ij}$	Residual error time for entire ray.
$i$	Angle of incidence.
$ij$	Subscript - from the $i$ 'th source to the $j$ 'th receiver.
$l_{ij}^{mn}$	Chord length.
$L_{ij}$	Total length of the ray.
$mn$	Superscript for parameter circle around point $m,n$ .
$m_0$	Slope of the linear $c(z)$ velocity.
$p$	Ray parameter.
$r$	Radius of any parameter circle.
$R$	Radius of curvature for the ray.
$s^{mn}$	Slowness matrix.
$\bar{s}^{mn}$	Slowness correction matrix.
$t_{ij}^{mn}$	Residence time.
$T_{ij}$	Calculated travel time for the ray $ij$ .
$\tilde{T}_{ij}$	Observed travel time for the ray $ij$ .
$w_{ij}^{mn}$	Weighting factor.
$x_i, z_j$	Offset to source, depth to receiver.

$x_m, z_m$

Offset and depth to parameter point mn.

$x_o, z_o$

Origin of the radius of curvature for the ray.



## 1. INTRODUCTION

One of the many goals of vertical seismic profiling (VSP) is to determine the lateral variations which occur away from the borehole. These lateral changes may reflect porosity, permeability, or facies changes within the rock unit. Such occurrences greatly influence the migration and accumulation of petroleum. Therefore, methods are needed to delineate these discrepancies between the borehole wall and the surrounding medium.

This investigation was geared at determining velocity inhomogeneities using only the first arrival times from a multiple offset VSP. The travel time through any medium is the integral of the slowness (reciprocal of the velocity) along the raypath. Unfortunately, this raypath itself is dependent upon the velocities within the medium. Thus, as posed, the problem is non-linear.

Linearizing this problem requires that the raypaths are known, which, in turn, necessitates a prior knowledge of the velocity structure. However, if we assume some general velocity trend for the medium, we can approximate the paths which the rays take. Then, the problem becomes one of finding the velocity perturbation from the assumed background velocity. Furthermore, we assume that all raypaths are not

influenced by this perturbation velocity; this assumption holds true for small perturbations. Since the rays are independent of the velocity perturbation, the problem becomes linear.

This research utilized two background models:

- 1) Constant velocity medium in which the rays form straight lines from the source to the receiver.
- 2) Linear  $c(z)$  velocity medium where the raypaths follow arcs along a circle.

The residual time is defined as the observed time minus the expected time as calculated from the velocity model. Fawcett (1983) utilized a Radon transform method for his seismic tomography of the slowness field from reflected residual travel times. Neumann (1981) used a least-squares inversion of residual travel times in his study on reflection seismics. Christofferson and Husebye (1979) applied a least-squares approach on P-wave residual times in a three-dimensional case. In contrast, McMechan (1983) and Mason (1981) opted for an algebraic reconstruction technique (ART). I have opted for the last approach, as well.

In comparison to a least-squares inversion, ART possesses several advantages:

- 1) ART programs are computationally faster and they are easier to program.
- 2) Constraints are easily incorporated into the program to accommodate any prior knowledge of the medium.
- 3) ART can be easily applied to any source/receiver geometry without difficulties.

ART has its origins within the medical field. Gordon, Bender, and Herman (1970) first introduced ART for the reconstruction of images from x-ray pictures. Later, Herman, Lent, and Rowland (1973) improved the early ART algorithms and Gordon (1974) summarized the various ART developments within the medical profession.

Several authors worked on reconstruction techniques which are applicable to the more general reconstruction problem rather than the specific x-ray case. Mersereau and Oppenheim (1974) and Mueller, Kaveh, and Wade (1979) applied ART to density reconstruction problems using the Fourier domain. Horn (1978) developed a density reconstruction algorithm for any arbitrary ray sampling scheme.

Geophysical tomography is relatively new. Dines and Lytle (1979) reconstructed pictures of electromagnetic properties in the region between a pair of boreholes. By assuming only straight raypaths, seismic velocity structures were obtained by both Mason (1981) and McMechan (1983). Mason concerned himself with inverting seismic data

shot between two boreholes, while McMechan imaged data shot from a borehole to a second borehole as well as to the surface.

The VSP model used in this paper consisted of ten point sources, which were equally spaced at 100 foot intervals along the surface. Similarly, a 100 foot spacing was used for the ten receivers placed down the borehole. No source or receiver resided at the top of the borehole (see Fig. 1). For a coordinate system, whose origin rested at the surface expression of the borehole, the x variable coincided with the surface offset distance and the z variable reflected the depth below the surface.

## 2. ALGEBRAIC RECONSTRUCTION TECHNIQUE - ART

The ART algorithm used here was adapted from Mason (1981). It involves a nine step process:

- 1) The medium is modeled by casting a set of overlapping circles on a uniform grid.
- 2) The total length of ray segments about a parameter is the sum of all the chord lengths formed by rays which pass through any given parameter circle.
- 3) The travel times associated with each of these chord lengths are determined by the velocity background model and summed.

- 4) The average slowness at the center of a parameter circle is the difference of 2) and 3). These outputs form a matrix indexed by  $mn$ .
- 5) Using the generated slowness matrix from 4), the expected travel times are calculated.
- 6) The residual time is the observed minus the calculated travel time.
- 7) This residual error time is equally distributed along the entire length of the ray.
- 8) A slowness correction matrix is computed in the manner of steps 2), 3), and 4).
- 9) Steps 5) through 8) are iterated.

### 2.1 Constant background

As stated earlier, this investigation used two different velocity backgrounds for the medium. First the constant velocity case will be discussed before going into the more complicated linear  $c(z)$  medium.

Using a constant velocity reference, the raypaths become straight lines from the  $i$ 'th source to the  $j$ 'th receiver. Denote the length of this ray as  $L_{ij}$ . Because the ray follows a straight course from  $(x_i, 0)$  to  $(0, z_j)$ , the raypath is represented by the equation:

$$z = - \left[ \frac{z_j}{x_i} \right] x + z_j. \quad (1)$$

Over the two-dimensional medium, a set of overlapping circles is drawn, whose centers form an uniform square grid (Fig. 2). These circles must completely cover the medium such that every point within the medium is contained in at least one of these parameter circles. The average slowness within any circle is assumed to be the slowness at the origin of the circle. These circles serve as a truncated least-distance averaging method which lies at the basis of Horn's algorithm (1978). Also, circles prove to be more convenient than a grid of squares.

Sources are positioned at the center of some, or all, of the circles along the surface and receivers are located at the origin of some, or all, of the circles at the borehole edge of the model. Clearly, the source or receiver spacing defines the largest possible grid size, or equivalently, the density of the parameter circles. Resolution is lost with too small of a density of parameter circles. Conversely, a greater grid density will increase the resolution only to the limit of the data.

Let the known value  $r$  denote the radius of any parameter circle. Then the circle, around the point  $(x_m, z_n)$ , is mathematically expressed as:

$$(x - x_m)^2 + (z - z_n)^2 = r^2. \quad (2)$$

If the ray in question intersects the parameter circle, then equation (1) and equation (2) will have two points in common. A quadratic equation is formed by substituting (1) into (2). The quadratic is solved using the quadratic formula. Should both points prove to be imaginary, then the ray fails to intersect the circle.

The chord length  $l_{ij}^{mn}$  is calculated using the distance formula. These chord lengths are formed by all rays  $ij$  which intersect a given parameter circle around the point  $mn$ . The total length of ray segments  $d^{mn}$ , around the parameter  $mn$ , is the sum of all these chord lengths.

$$d^{mn} = \sum_{ij} l_{ij}^{mn}. \quad (3)$$

Every ray  $ij$ , which passes through a parameter circle  $mn$ , will have a residence time  $t_{ij}^{mn}$  within that circle as calculated from the observed travel time  $\tilde{T}_{ij}$  and a weighting factor  $w_{ij}^{mn}$ .

$$t_{ij}^{mn} = \tilde{T}_{ij} w_{ij}^{mn}. \quad (4)$$

This weighting factor depends on the background velocity and can be viewed as the ratio of the expected time spent inside the circle to the total expected time of the ray. For a constant  $c_0$  velocity background:

$$w_{ij}^{mn} = \frac{\left[ \frac{l_{ij}^{mn}}{c_o} \right]}{\left[ \frac{l_{ij}}{c_o} \right]} = \frac{l_{ij}^{mn}}{l_{ij}}. \quad (5)$$

The total time spent about a parameter point mn is the sum of all the residence times. The average slowness at the point mn is given by:

$$s_{mn} = \frac{\sum_{ij} t_{ij}^{mn}}{\sum_{ij} l_{ij}^{mn}}. \quad (6)$$

## 2.2 Constant background - Iterative algorithm

An iterative technique is applied to improve upon this first guess model. First, a forward model is needed to compute an estimated travel time. Using straight raypaths, the ray is divided into equal segments  $\Delta l$ . The slowness along the entire segment length is assumed to equal the slowness at the midpoint of the segment, which is estimated by fitting a two-dimensional parabola to the surrounding four points of the slowness matrix. The estimated travel time  $T_{ij}$  is the sum of the slowness along the raypath.



$$T_{ij} = \sum_{(x_i, 0)}^{(0, z_j)} s(x, z) \Delta l. \quad (7)$$

The total residual travel time  $E_{ij}$  along ray  $ij$  is given by:

$$E_{ij} = \tilde{T}_{ij} - T_{ij}. \quad (8)$$

This residual error time is equally distributed along the length of the ray. The slowness correction matrix is the ratio of the total error times about a parameter to the total length of the ray segments.

$$\tilde{s}^{mn} = \frac{\sum_{ij} e_{ij}^{mn}}{\sum_{ij} l_{ij}^{mn}}, \quad \text{where } e_{ij}^{mn} = E_{ij} \left[ \frac{l_{ij}^{mn}}{L_{ij}} \right]. \quad (9)$$

This slowness correction matrix is added to the previous slowness matrix to obtain an updated model. Iteration is performed by computing a new correction matrix, based on the current slowness model, until the mean square of the residual times reaches a steady state.

$$\sum_{ij}^{\text{old}} (E_{ij})^2 - \sum_{ij}^{\text{new}} (E_{ij})^2 < \epsilon. \quad (10)$$

### 2.3 Linear $c(z)$ medium

For a linear  $c(z)$  medium, the raypaths are no longer straight, but instead are curved. The local radius of curvature is derived using Snell's Law.

$$\frac{\sin i}{c(z)} = p = \text{constant.} \quad (11)$$

Taking the derivative of the ray parameter, and noting that the derivative of any constant is zero, we find that

$$dp = \frac{\partial p}{\partial i} di + \frac{\partial p}{\partial z} dz, \quad (12)$$

or

$$0 = \frac{\cos i}{c(z)} di - \frac{\sin i}{c^2(z)} \frac{dc(z)}{dz} dz. \quad (13)$$

From the geometry shown in Fig. 3:

$$dS = R di, \quad \text{and} \quad \cos i = \frac{dz}{dS}. \quad (14)$$

By combining the two equations (14), we conclude that

$$di = \frac{dz}{R \cos i}. \quad (15)$$

Substituting (15) into (13):

$$0 = \frac{dz}{R c(z)} - \frac{\sin i}{c^2(z)} \frac{dc(z)}{dz} dz, \quad (16)$$

or

$$\frac{1}{R} = \frac{\sin i}{c(z)} \frac{dc(z)}{dz} = p \frac{dc(z)}{dz}. \quad (17)$$

So for a linear velocity  $c(z) = c_0 + m_0 z$ , the radius of curvature becomes a constant, which implies that the raypath is simply the arc along some circle; that is,

$$\frac{1}{R} = p m_0. \quad (18)$$

Using the Wiechert-Herglotz integral (Aki and Richards, 1980), the ray parameter can be determined (See appendix A). The result is

$$p = \frac{2 m_0 x_i}{\sqrt{[m_0^2 x_i^2 + c_0^2 + c^2(z_j)]^2 - 4 c_0^2 c^2(z_j)}}. \quad (19)$$

From the ray parameter, the radius of curvature becomes known using equation (18). With two points on this circular path known, namely the shot and receiver locations, the ray follows a path on the circle:

$$(x - x_0)^2 + (z - z_0)^2 = R^2. \quad (20)$$

Using the geometry in Fig. 4, the center of the circle can be determined:

$$|x_0| = R \cos(i + \alpha); \quad (21)$$

$$|z_0| = R \sin i. \quad (22)$$

Both angles are calculated from the geometry. The results are

$$\sin \frac{\alpha}{2} = \frac{x_i^2 + z_j^2}{2R}; \quad (23)$$

$$\tan(i + \frac{\alpha}{2}) = \frac{x_i}{z_j}. \quad (24)$$

Thus for a linear  $c(z)$  medium, the rays are arcs of a circle. The overall length of the ray is:

$$L_{ij} = R\alpha. \quad (25)$$

Over the two-dimensional medium, a grid of overlapping circles is

superimposed. Any ray will intersect a circle provided that:

$$|d - R| < r, \quad \text{where } d^2 = (x_m - x_0)^2 + (z_m - z_0)^2. \quad (26)$$

The arc length  $l_{ij}^{mn}$  formed by the ray  $ij$ , within the circle  $mn$ , is computed using the law of cosines (Fig. 5).

$$\cos \frac{\beta}{2} = \frac{R^2 + d^2 - r^2}{2 R d}; \quad (27)$$

$$l_{ij}^{mn} = R \beta. \quad (28)$$

The total ray distance  $d^{mn}$ , about a given parameter, is the sum of all the arc lengths.

$$d^{mn} = \sum_{ij} l_{ij}^{mn}. \quad (29)$$

Every ray  $ij$ , which passes through a parameter circle  $mn$ , will have a residence time  $t_{ij}^{mn}$  within that circle as calculated from the observed travel time  $T_{ij}$  and a weighting factor  $w_{ij}^{mn}$ .

$$t_{ij}^{mn} = T_{ij} w_{ij}^{mn}. \quad (30)$$

The weighting factor is the ratio of the expected time spent inside

the parameter circle to the overall travel time for the entire ray.

$$v_{ij}^{mn} = \frac{\left[ \frac{l_{ij}^{mn}}{c(z_n)} \right]}{T_{ij}}. \quad (31)$$

Here  $c(z_n)$  is the velocity at the origin of the parameter circle and  $T_{ij}$  is the theoretical travel time of the ray in the assumed linear background (see appendix B).

$$T_{ij} = \frac{1}{c_0} \ln \left[ \frac{c(z_j) (1 + \sqrt{1 - p^2 c_0^2})}{c_0 (1 + \sqrt{1 - p^2 c^2(z_j)})} \right]. \quad (32)$$

The average slowness at the point mn is given by:

$$s^{mn} = \frac{\sum_{ij} t_{ij}^{mn}}{\sum_{ij} l_{ij}^{mn}}. \quad (33)$$

#### 2.4 Linear $c(z)$ medium - Iterative algorithm

The slowness matrix can be improved by an iteration technique. The curved ray is divided into equal segments  $\Delta l$ . The slowness along the entire segment length is assumed to equal the slowness at the midpoint of the segment, which is estimated by fitting a two-dimensional para-

boloid to the surrounding four points of the slowness matrix. An estimated travel time is computed by summing the slownesses at the mid-points of the segments.

$$T_{ij} = \sum_{(x_i, 0)}^{(0, z_j)} s(x, z) \Delta l. \quad (34)$$

The total residual time  $E_{ij}$  along the ray  $ij$  is given by:

$$E_{ij} = \tilde{T}_{ij} - T_{ij}. \quad (35)$$

This residual error time is distributed equally along the raypath. The slowness correction matrix is the ratio of the sum of the local residual times to the sum of the arc lengths around each parameter:

$$\tilde{s}^{mn} = \frac{\sum_{ij} e_{ij}^{mn}}{\sum_{ij} l_{ij}^{mn}}, \quad \text{where} \quad e_{ij}^{mn} = E_{ij} \left[ \frac{l_{ij}^{mn}}{L_{ij}} \right]. \quad (36)$$

This slowness correction matrix is added to the slowness matrix to obtain a revised slowness model. Iteration is performed, by computing a new correction matrix based on the updated slowness model, until the mean square of the residual times reaches a steady state:

$$\sum_{ij} (E_{ij})^2_{\text{old}} - \sum_{ij} (E_{ij})^2_{\text{new}} < \epsilon. \quad (37)$$

### 3. TESTING THE ALGORITHMS

Both the constant and linear velocity background ART algorithms were tested using synthetic data sets. For a given slowness model, the travel times were generated using the forward modeling scheme in either the constant or linear velocity case. The slowness was integrated along either straight or circular paths as dictated by the general velocity trend of the input velocity model. Where the velocity increased linearly with  $x$  instead of  $z$ , the reciprocity principle of interchanging the shot and receiver locations was applied. Such data was calculated by interchanging the  $x$  and  $z$  variables and using the technique of section 2.4 to compute the synthetic data.

Clearly, the synthetic data does not correspond exactly to the perturbations which would be measured in the real case, but instead, the travel times represent a first order approximation for relatively small amplitude velocity anomalies. Therefore, my results test the accuracy of the reconstruction method and not the validity of linearizing the



problem.

#### 4. RESULTS

ART produces the best tomographical results when the velocity function is smoothly varying. Using synthetic data sets, accurately inverted velocity values occurred within the model, but the velocity values varied from the synthetic input near the edges of the model (Fig. 6, 7, 8, 9, 10, 11).

The greatest deviation occurred near the origin (Fig 6b, 7b, 8b, 11b, 11c). The first velocity down the well is erroneously high while the first velocity along the surface is erroneously low. The apparent cause of this phenomenon rests within the raypaths themselves and the way in which the ART algorithm handles these raypaths.

The first parameter down the well reflects the slownesses along the rays from all ten shot locations. However, the shortest raypath length most accurately reflects the true velocity at this point, while the longer rays reflect less of the velocity in question and more of the velocities further away. Because the ART algorithm equally weights all rays, regardless of their relative lengths, the slowness down the hole reflects the velocity change across the surface of the model. Appropriate constraints down the well will eliminate this problem, since the slowness in a borehole are usually known from the sonic log (Fig 11d).

Along the edges, the velocity values fluctuated from the synthetic model. These deviations resulted from two factors. First, the erroneous origin velocities greatly influence the surface and borehole edges. Second, the diagonal edge parameters are poorly constrained.

Unconstrained parameters are defined by only one ray. All parameters within my model had at least three rays defining each parameter. However, along the diagonal edge, these three rays are nearly identical and as such, they are defined by nearly the same parameters. Therefore, these rays fail to be completely independent of each other. Thus, the parameters along the diagonal edge are poorly constrained. In unconstrained cases, ART tends to average the velocities equally along the raypath resulting in resolution problems.

By using a delta function as the input velocity structure (Fig 9), we can better illustrate this resolution problem. Resolution along the raypaths is poor, but between the rays, the resolution increases. This accounts for the skewness of the inverted delta function into an elliptical form elongated along the dominant raypath direction. Still, the location of the slowness delta point is accurately defined, though not its true velocity value.

This poor resolution along the raypaths contributes to uniqueness problems (Fig 10). In general, an infinite number of models can produce the same travel time data. ART converges to the model which is the closest to the assumed background velocity and not necessarily a

representative of the true medium.

Uniqueness requires that all the slowness parameters are over constrained; that is more than one ray intersects each parameter circle. Furthermore, these rays must be independent. A close examination of my model reveals that at least three rays intersect each parameter; however, these rays travel approximately along the same direction and thus, these rays reflect many of the same slowness parameters. Clearly, these rays are not independent of each other.

The back-projected algorithm along curved rays was tested using synthetic data generated on linear trending, velocity models. In each case, the curved ART algorithm accurately reconstructed the synthetic models (Fig. 12, 13, 14).

#### 5. PIERRE SHALE EXPERIMENT

The multiple offset VSP, which was taken by the CSM Exploration Research Laboratory of the Geophysics Department, provided a real data test of the algorithms. Field work was done, in November 1980, at the CSM test site in northeastern Colorado, about five miles south of Brush Colorado (Southwest 1/4, Section 28, Township 3N, Range 55W). Sixta (1982) describes the data aquisition and data processing of this VSP experiment.

This site was chosen for its simple geologic setting. A 40 foot

thick layer of eolian sand rests on the surface. Beneath this sand layer, a 40 foot thick layer of clay grades into the Pierre Shale below. These thicknesses vary laterally away from the borehole. Because the upper 1000 feet of the Pierre Shale is well noted for its homogeneous nature, refracted events should not appear on the records and therefore, the direct ray will be the first arrival.

The field layout is sketched in Fig. 15. Geophones were spaced down the cemented well every 100 feet within the interval between 400 and 1000 feet. Dynamite, placed in shot holes at a depth of 100 feet deep, were shot at 200 foot intervals across the surface to a distance of 1400 feet from the borehole. The travel times were picked at the first trough on the records (Fig. 16) and are tabulated in the table below.

Table 1: Travel times in msec.

Depth in ft.	Horizontal offset in ft.						
	200	400	600	800	1000	1200	1400
400	50.25	62.00	82.75	106.25	133.50	160.00	187.00
500	64.50	74.00	91.75	113.00	138.50	163.50	189.75
600	78.75	86.50	101.75	121.00	144.50	168.00	193.50
700	92.25	99.00	112.25	129.75	151.50	174.00	198.25
800	106.00	111.75	123.50	139.25	159.50	180.75	203.50
900	119.25	124.50	135.00	149.00	168.00	188.00	210.00
1000	133.50	138.00	147.00	160.00	177.75	196.50	217.00

Picking the arrival times at the first trough results in a lag time of about 3 msec. from the true onset of the waveform. This error in the travel time corresponds to a similar error in the velocity value. The

travel time is the integral of the slowness along the raypath.

$$t = \int \frac{1}{c} dL, \quad \text{or} \quad t \approx \frac{L}{c}. \quad (38)$$

Differentiating (38), we obtain

$$dt \approx -L \frac{dc}{c^2}. \quad (39)$$

Dividing (38) into (39), yields the result

$$\frac{dt}{t} \approx -L \frac{dc}{c}. \quad (40)$$

By setting  $dt=3$  msec. and noting that  $t$  ranges from 50.25 to 217.0 msec., the true velocity values range from 6.0 to 1.3% faster than those which are shown in the reconstructed fields.

The Pierre Shale is well noted for its homogeneous nature; however, our reconstructions fail to support this characteristic. Imaging was performed both without parameter constraints and with constraining the slowness parameters down the borehole to within five percent of the measured slowness values off the sonic log.

Both the constrained (Fig. 18a, 18b) and the unconstrained (Fig. 17a, 17b) reconstructions reveal a questionable high velocity cell near the surface. Although the sonic log for the well records a velocity of

6250 ft/sec at a depth of 100 feet, the reconstructed high, only 600 feet away, reaches 11,900 ft/sec for the unconstrained case and 12,000 ft/sec for the constrained case. However, these velocity highs consisted of a single, poorly-constrained parameter along the surface, which clearly introduces uncertainty into this velocity value.

By eliminating any poorly constrained parameters along the surface, the imaging process is improved (Fig. 19, 20). These errant velocity values were ignored only when the reconstructed velocity field was contoured, and thus, they were used throughout the reconstruction algorithm. A similar step was applied to the reconstructions using circular rays based on the linear velocity trend exhibited by the sonic log (Fig. 21, 22). Each reconstruction shows a high velocity ridge of 8,000 ft/sec. hovering between a horizontal offset of 200 to 900 feet at a depth around 200 to 300 feet. Additionally, a low velocity cell exists at 100 foot offset and a depth of 500 to 800 feet. This low cell fluctuates between velocities of 7,000 to 7,200 ft/sec. depending upon the reconstruction conditions.

To test the validity of these reconstructions, the observed travel times were compared to theoretical data from a linearly increasing medium. This synthetic model, based on sonic log information, initially started at a velocity of 7,000 ft/sec. and increased to 8,000 ft/sec. at the total depth of the well. For comparison, both the synthetic and the Pierre Shale VSP travel times were plotted for each geophone posi-

tion (Fig. 23). Where the synthetic curve arrives after the observed times, a velocity increase is required. Where the observed times lag behind the synthetic, lower velocities are expected. Relative to the synthetic model, we should expect higher velocities at the large offset distances, but lower velocities at small offsets and large depth.

Because surface velocities are typically very slow, the high surface velocity is contrary to expectations. Three feasible explanations arise for this velocity anomaly. Either the velocity structure exists, or the data or the collection of the data is questionable, or the basic theory is inadequate for the earth conditions exhibited by the Pierre Shale. Poorly placed shot locations could result in an artificial high at the surface, if the errant shot locations resulted in a shorter ray-path.

A more feasible explanation arises from the strong anisotropy exhibited by the Pierre Shale. After using the same data collected near Brush, Colorado, White, Martineau-Nicoletis, and Monash (1983) concluded that the horizontal velocity component was 10 to 20% faster than the vertical velocity component. Qualitatively, the rays from the large offset sources possess mostly a horizontal component and thus, should exhibit a greater than expected velocity. Similarly, the deeper traveling rays are mostly vertical and would travel at the slower velocity. Therefore, the anisotropy of the Pierre Shale explains the high surface velocity and the low velocity cell at depth of the reconstructed velo-

city fields.

## 6. CONCLUSIONS

Algebraic reconstruction technique (ART) concentrates on the production of a reconstructed field whose projected data (travel times) agree with the observed data. This reconstructed field is modified by altering the data for each ray such that when this data is back-projected, the new image agrees with the original data.

ART possesses many inherent advantages. The flexibility of the algorithm easily allows for the incorporation of constraints. For example, sonic log information predetermines the velocity parameters down the borehole. This flexibility also permits the application of ART to any field setup of sources and receivers.

With noiseless data, ART picks a projection which agrees with the observed data. It is not in ART's nature to introduce spurious images on good data sets. However, the resolution of the image is affected by the orientation of the anomaly relative to the direction of the rays. While good resolving power occurs perpendicular to the rays, ART tends to smooth the image along the direction of the rays.

With noisy data, ART can produce single point anomalies of highly unrealistic velocities among the poorly-constrained parameters along the edges of the model. ART will produce a reasonable reconstructed velo-



city field when constraints are incorporated from the well log information or by simply ignoring any poorly-constrained parameters within the image. Lastly, data, which was collected over a strongly anisotropic medium, will result in poor velocity reconstructions, because such data

## REFERENCES

- Aki, R. and P. G. Richards, Quantitative Seismology: Theory and Methods, Vol. II, W. H. Freeman and Company: San Francisco, (1980).
- Christofferson, A. and E. S. Husebye, "On 3-D inversion of P-wave time residuals option for geological modeling," J. Geophys. Res., 84 (1979) 6168-6176.
- Dines, K. A. and R. J. Lytle, "Computerized geophysical tomography," Proc. IEEE, 67 (1979) 1065-1073.
- Fawcett, J. A., "I. Three dimensional ray-tracing and ray-inversion in layered media. II. Inverse scattering and curved ray tomography with applications to seismology." PhD Thesis: California Institute of Technology, Pasadena, (1983) 229 pp.
- Gordon, R., "A tutorial on ART," IEEE Trans. Nucl. Sci., NS-21 (June 1974) 78-93.
- Gordon, R., R. Bender, and G. T. Herman, "An algebraic reconstruction technique (ART) for 3-D electron microscopy and x-ray photography," J. Theor. Biol., 29 (1970) 471-518.
- Herman, G. T., A. Lent, and S. W. Rowland, "ART: Mathematics and applications," J. Theor. Biol., 42 (1973) 1-32.

- Horn, B. K. P., "Density reconstruction using arbitrary ray-sampling schemes," Proc. IEEE, 66 (1978) 551-562.
- Mason, I. M., "Algebraic reconstruction of a two-dimensional velocity inhomogeneity in the High Hazles seam of Thoresby colliery," Geophysics, 46 (1981) 298-308.
- McMechan, G. A., "Seismic tomography in boreholes," Geophys. J., 74 (1983) 601-621.
- Mersereau, R. M., and A. V. Oppenheim, "Digital reconstruction of multidimensional signals from their projections," Proc. IEEE, 62 (1974) 1319-1338.
- Mueller, R. K., M. Kaveh, and G. Wade, "Reconstructive tomography and applications to ultrasonics," Proc. IEEE, 67 (1979) 567-587.
- Neumann, G., "Determination of lateral inhomogeneities in reflection seismics by inversion of travel time residuals," Geophys. Prosp., 29 (1981) 161-177.
- Sixta, D. P., "Comparision and analysis of downgoing waveforms from land seismic sources," M.S. Thesis: Colorado School of Mines, Golden, (1982) 451 pp.
- White, J. E., L. Martineau-Nicoletis, and C. Monash, "Measured anisotopy in Pierre Shale," Geophys. Prosp., 31 (1983) 709-725.

## APPENDIX A: RAY PARAMETER DERIVATION

The ray parameter within a linear  $c(z)$  medium is determined from the Wiechert-Herglotz integral (Aki and Richards, 1980).

$$x_i = p \int_0^{z_j} \frac{dz}{\sqrt{\eta^2 - p^2}}, \quad (\text{A-1})$$

where  $\eta = \frac{1}{c(z)}$  is the slowness,

$x_i$  is the source offset,

$z_j$  is the receiver depth.

The medium is assumed to possess a linear velocity structure.

$$c(z) = c_0 + m_0 z; \quad c_0 = c(0), \text{ the surface velocity.} \quad (\text{A-2})$$

Substituting (A-2) into (A-1), we obtain

$$x_i = p \int_0^{z_j} \frac{(c_0 + m_0 z) dz}{\sqrt{1 - p^2 (c_0 + m_0 z)^2}}. \quad (\text{A-3})$$

The integration may be carried out explicitly. The result is

$$x_i = \frac{1}{m_0 p} \sqrt{1 - p^2 c^2(z)} \Big|_{z=0}^{z=z_j}, \quad (\text{A-4})$$

$$x_i = \frac{1}{m_0 p} \left[ \sqrt{1 - p^2 c^2(z_j)} - \sqrt{1 - p^2 c_0^2} \right]. \quad (\text{A-5})$$

Squaring both sides, we find

$$(x_i p m_0)^2 = (1 - p^2 c_0^2) + (1 - p^2 c^2(z_j)) - 2 \sqrt{(1 - p^2 c_0^2)(1 - p^2 c^2(z_j))}, \quad (\text{A-6})$$

or

$$(x_i p m_0)^2 - 2 + p^2 (c_0^2 + c^2(z_j)) = -2 \sqrt{(1 - p^2 c_0^2)(1 - p^2 c^2(z_j))}. \quad (\text{A-7})$$

Again squaring both sides, we find

$$p^4 [m_0^2 x_i^2 + c_0^2 + c^2(z_j)]^2 - 4 c_0^2 p^2 [m_0^2 x_i^2 + c_0^2 + c^2(z_j)] + 4 = 4 (1 - p^2 c_0^2)(1 - p^2 c^2(z_j)), \quad (\text{A-8})$$

or

$$p^4 [m_0^2 x_i^2 + c_0^2 + c^2(z_j)]^2 - 4 c_0^2 p^2 [m_0^2 x_i^2 + c_0^2 + c^2(z_j)] - 4 p^2 m_0^2 x_i^2 = 0. \quad (\text{A-9})$$

Solving for  $p$ , we obtain

$$p^2 = 0, \quad p^2 = \frac{4 m_0^2 x_i^2}{[m_0^2 x_i^2 + c_0^2 + c^2(z_j)]^2 - 4 c_0^2 c^2(z_j)}. \quad (\text{A-10})$$

However, the ray parameter must be positive for a linearly increasing medium. Thus, we conclude that

$$p = \frac{2 m_0 x_i}{\sqrt{[m_0^2 x_i^2 + c_0^2 + c^2(z_j)]^2 - 4 c_0^2 c^2(z_j)}}. \quad (A-11)$$

## APPENDIX B: TRAVEL TIME CALCULATION

The travel time in a linear  $c(z)$  medium is calculated by the Wiechert-Herglotz inversion method (Aki and Richards, 1980).

$$T_{ij} = \int_0^{z_j} \frac{dz}{c(z) \sqrt{1 - p^2 c^2(z)}}. \quad (B-1)$$

We introduce the new variable of integration  $\theta$ :

$$p c(z) = \sin \theta, \quad (B-2)$$

$$\sqrt{1 - p^2 c^2(z)} = \cos \theta. \quad (B-3)$$

Differentiating (B-3), we obtain

$$p m_0 dz = \cos \theta d\theta. \quad (B-4)$$

Substituting (B-2) and (B-4) into (B-1) yields:

$$T_{ij} = \frac{1}{m_0} \int \frac{d\theta}{\sin \theta}, \quad (B-5)$$

$$T_{ij} = \frac{-1}{m_0} \ln [\csc \theta + \cot \theta]. \quad (B-6)$$

In terms of  $z$ , this yields the result

$$T_{ij} = \frac{1}{m_0} \ln \left[ \frac{1 + \sqrt{1 - p^2 c^2(z)}}{pc(z)} \right] \Big|_{z=z_j}^{z=0}, \quad (B-7)$$

$$T_{ij} = \frac{1}{m_0} \ln \left[ \frac{c(z_j) (1 + \sqrt{1 - p^2 c_0^2})}{c_0 (1 + \sqrt{1 - p^2 c^2(z_j)})} \right]. \quad (B-8)$$



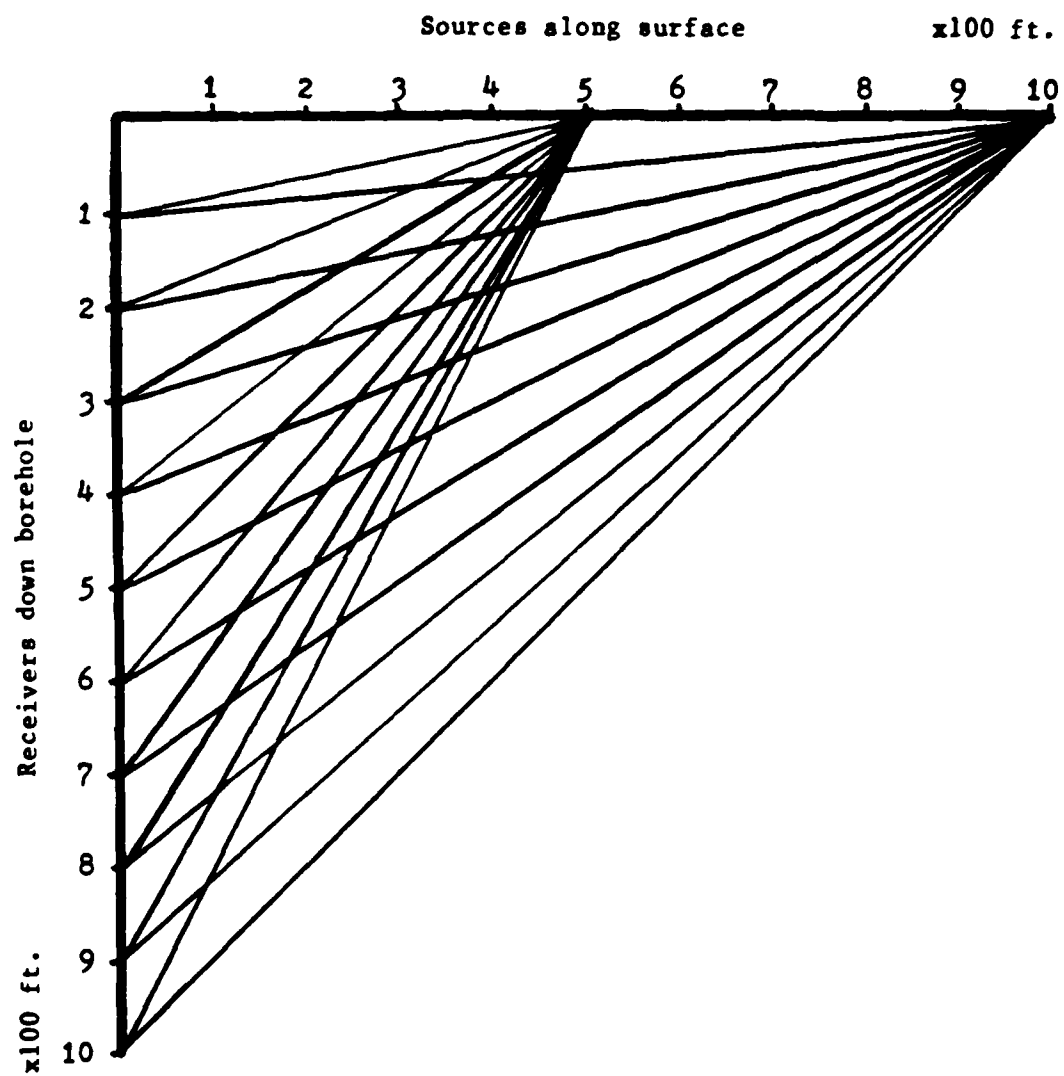


Figure 1. Multiple offset VSP geometry.

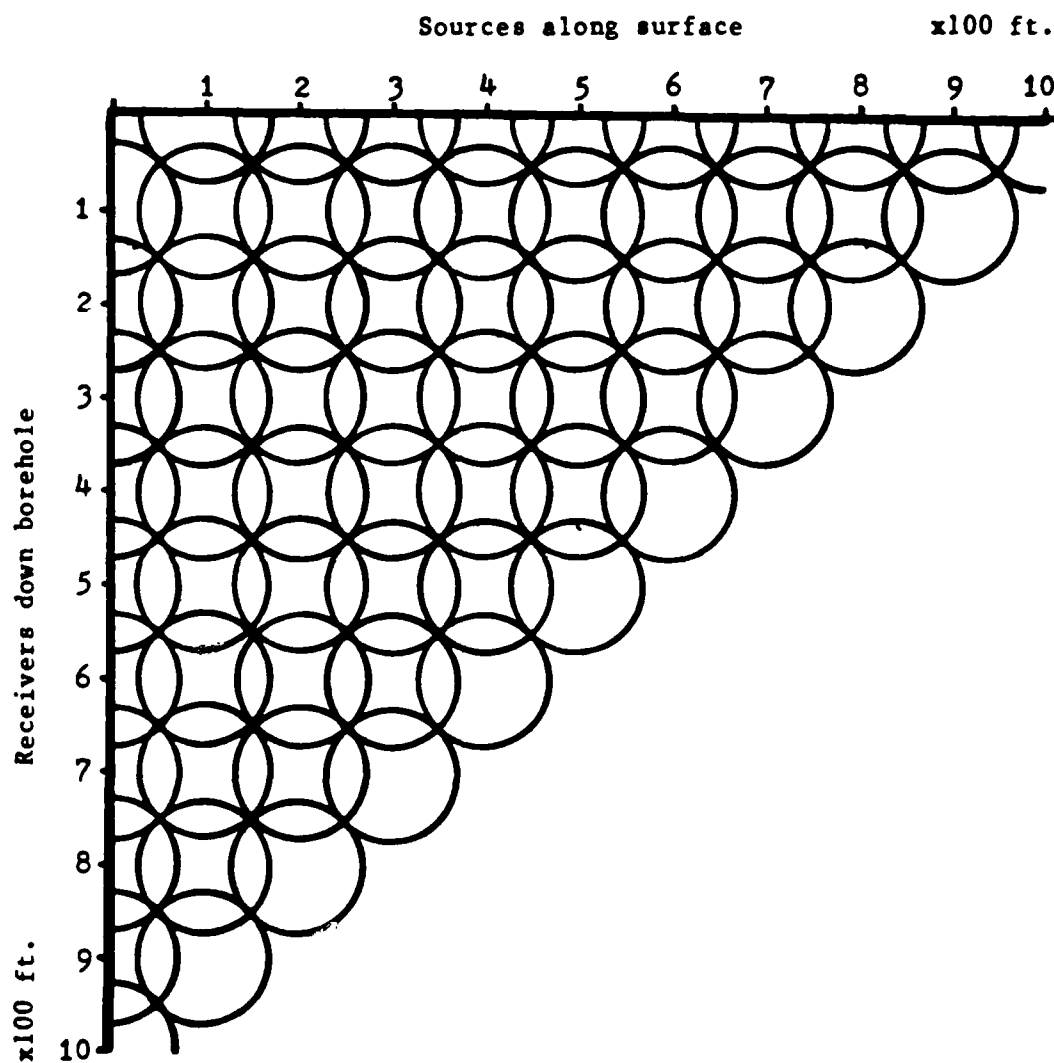


Figure 2. Modeling the medium using overlapping circles.

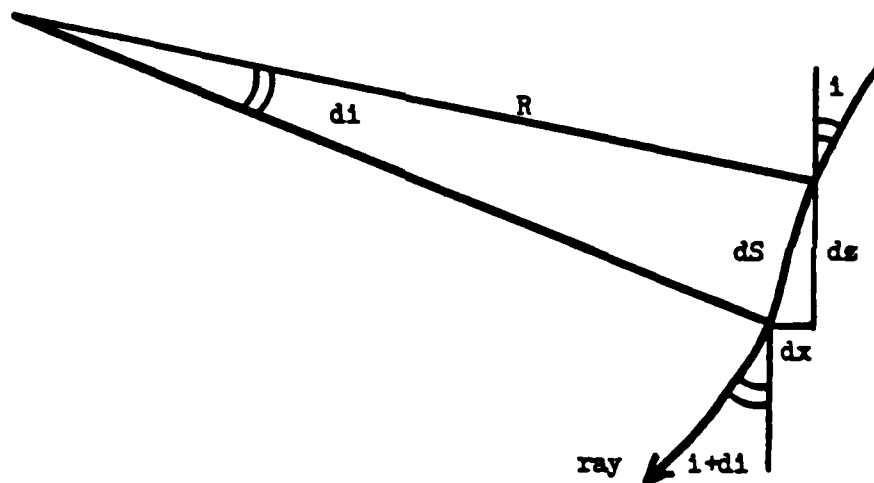


Figure 3. Derivation of the local radius of curvature.

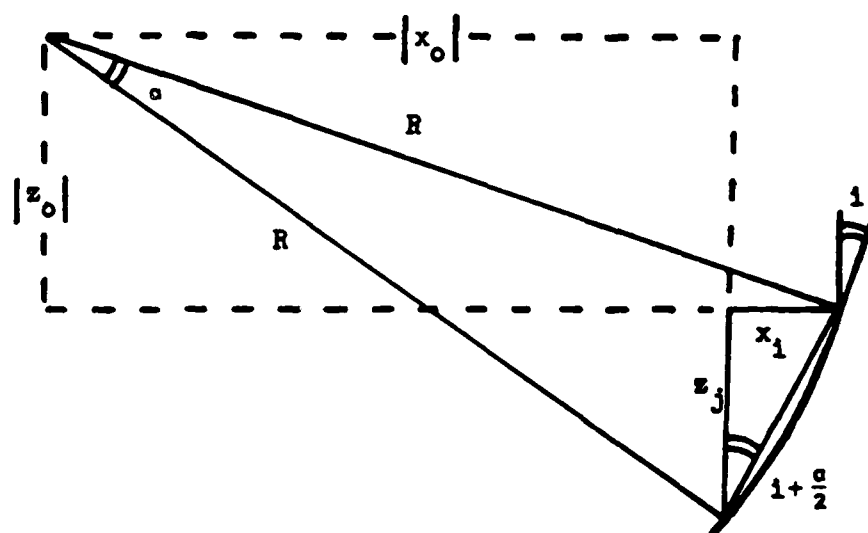


Figure 4. Origin determination.

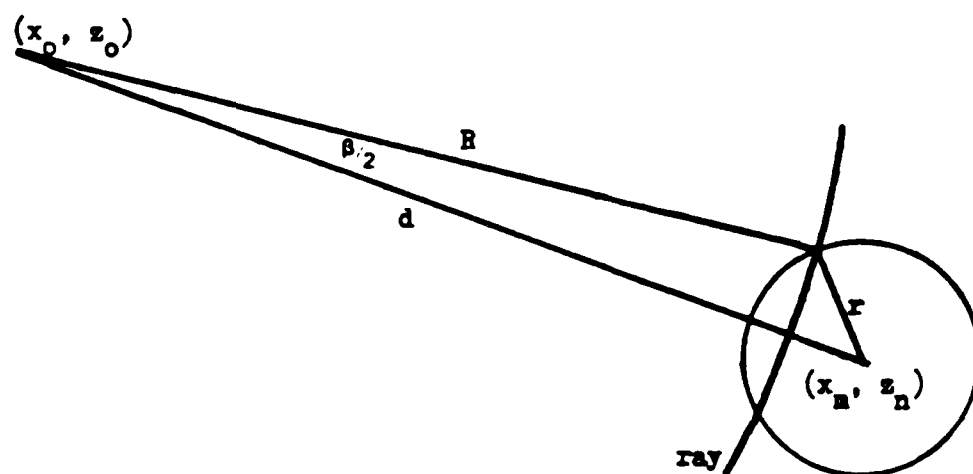
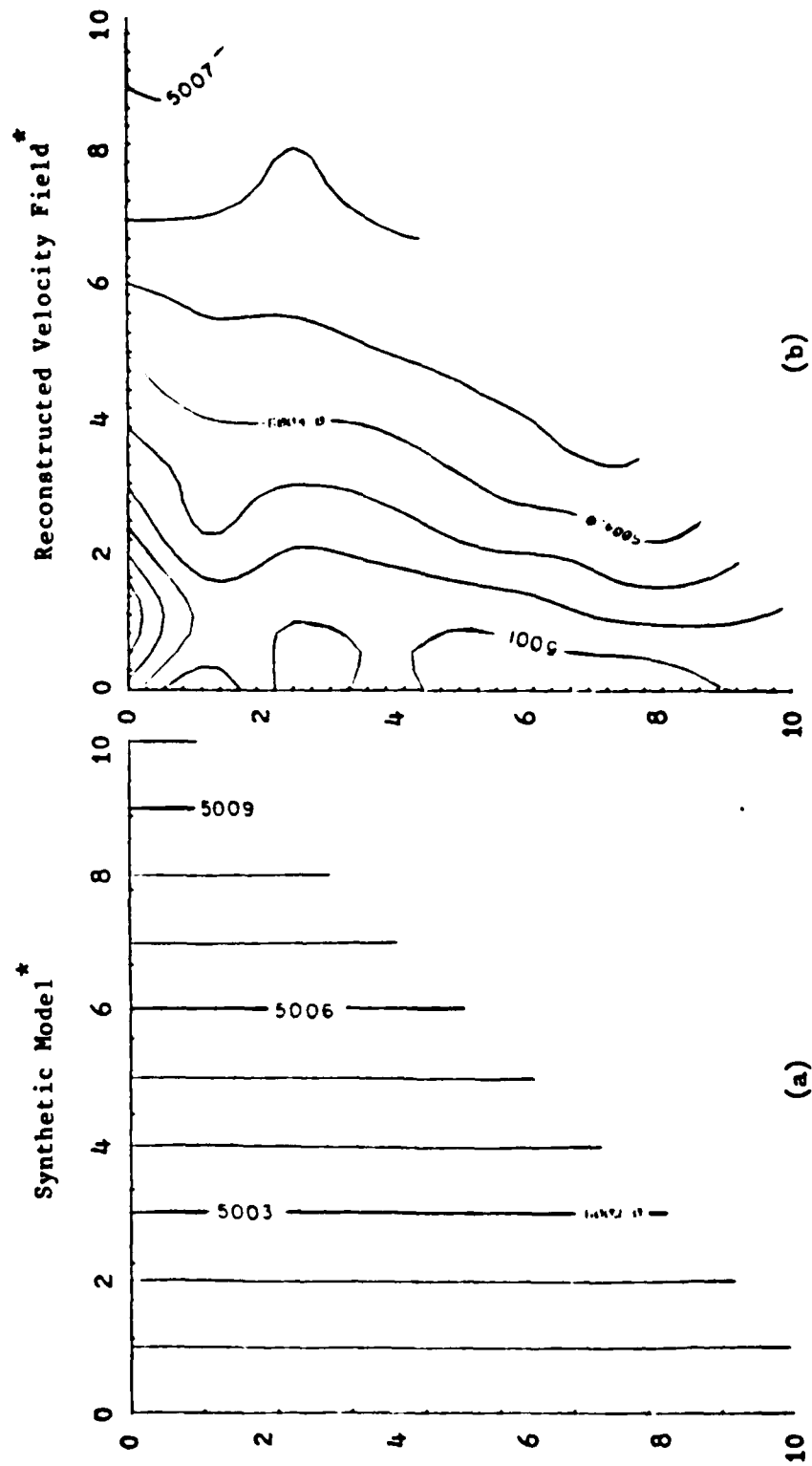
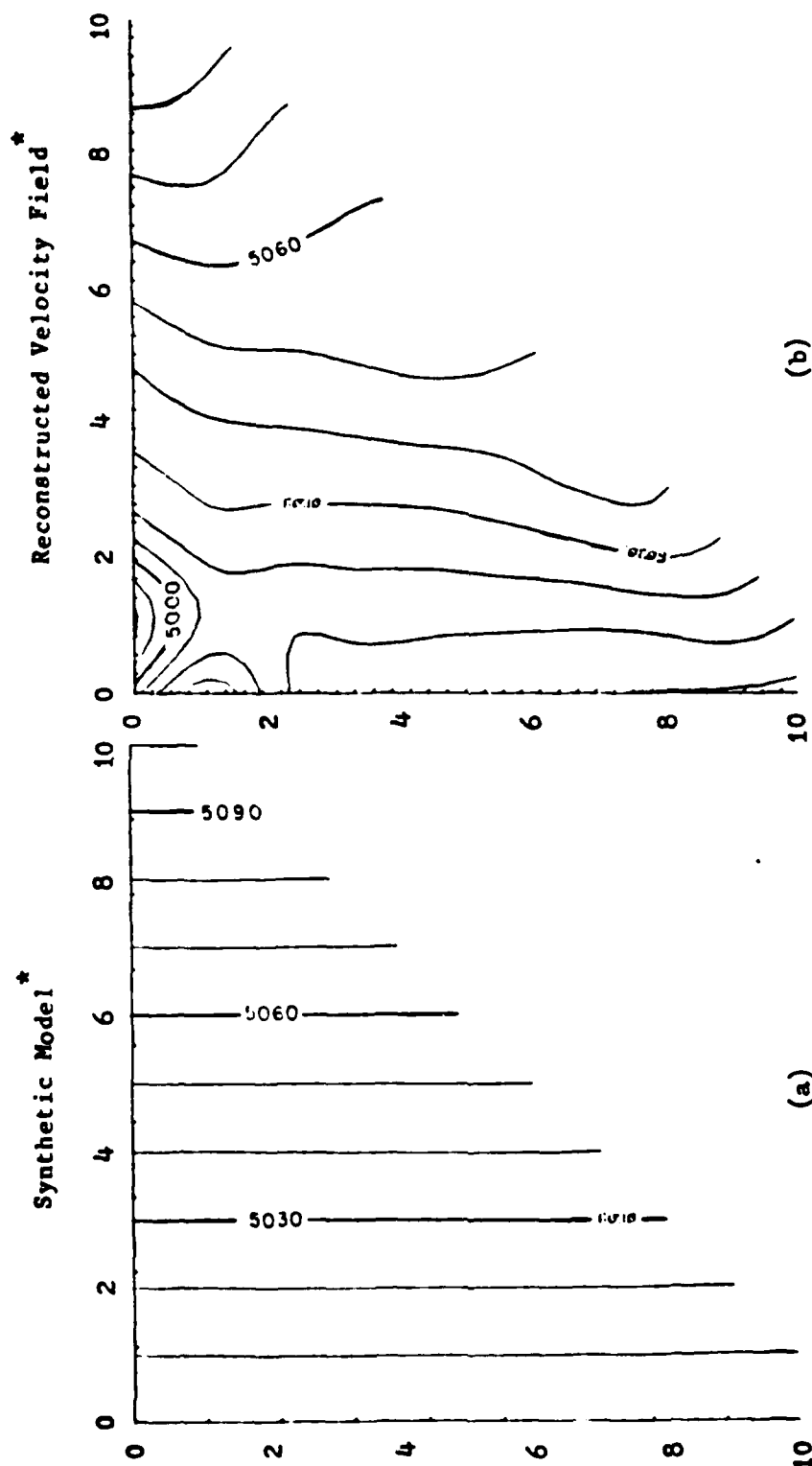


Figure 5. Arc length determination.



\* Travel times calculated using curved rays based on a background velocity  $- v(x) = 5000 + .01(x_i)$ .  
 \* After 7 iterations using straight rays.

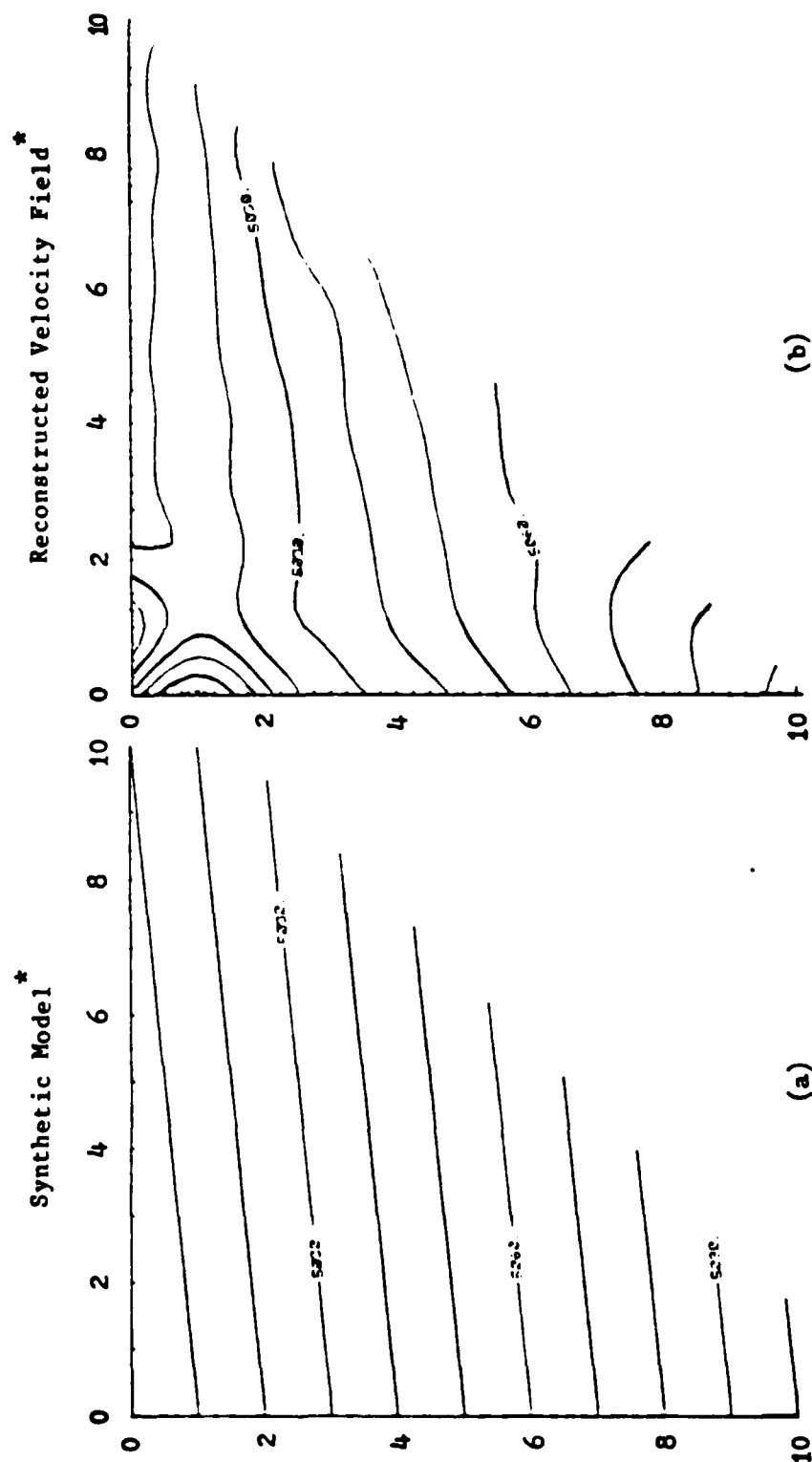
Figure 6. Velocity increasing with  $x$ .



\* Travel times calculated using curved rays based on a background velocity  $-v(x) = 5000 + .1(x_i)$ .

\* After 9 iterations using straight rays.

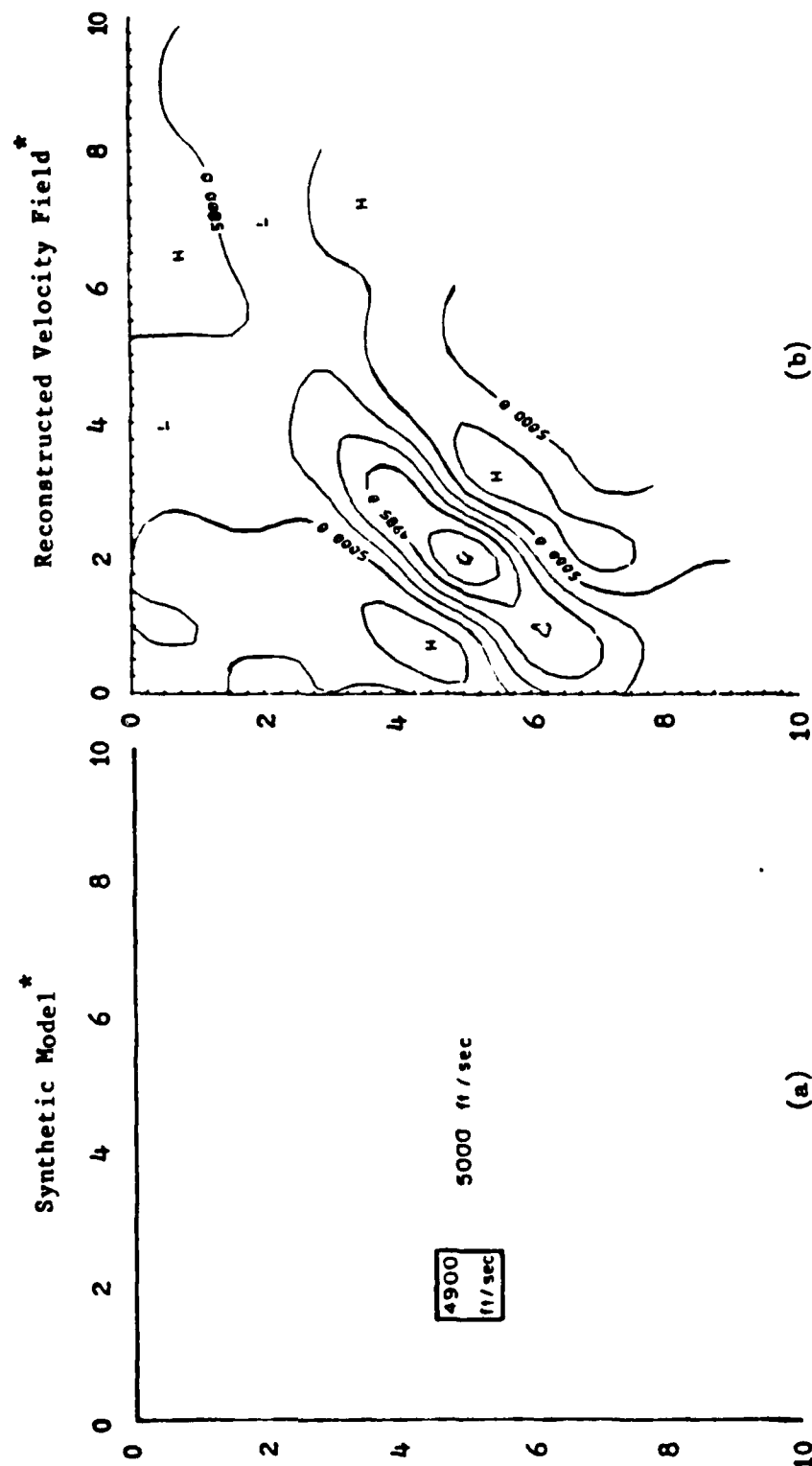
Figure 7. Velocity increasing with  $x$ .



\* Travel times calculated using straight rays. \* After 11 iterations using straight rays.

Figure 8. Dipping model.





\* Travel times calculated using straight rays. \* After 12 iterations using straight rays.

Figure 9. Model of a low velocity anomaly.

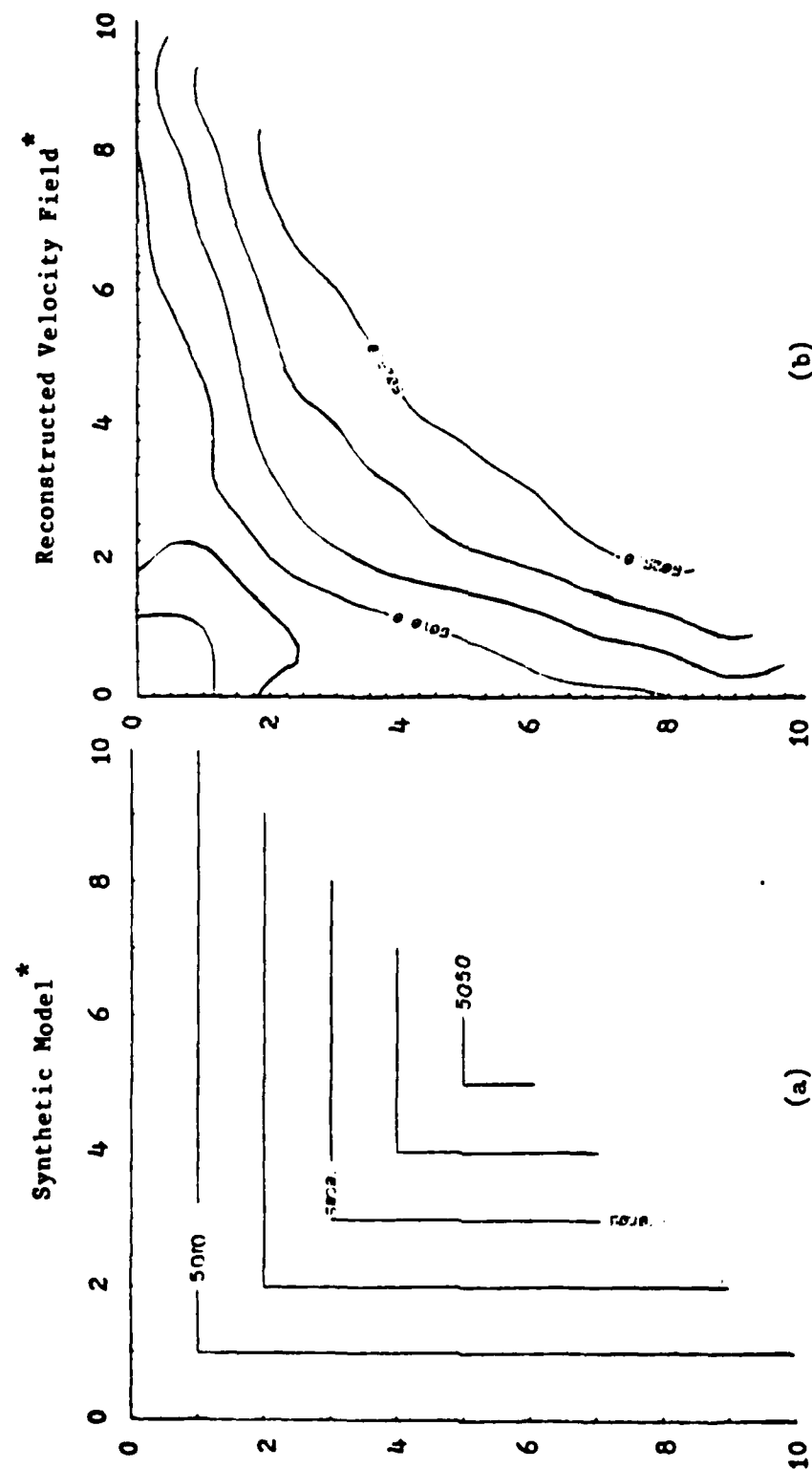
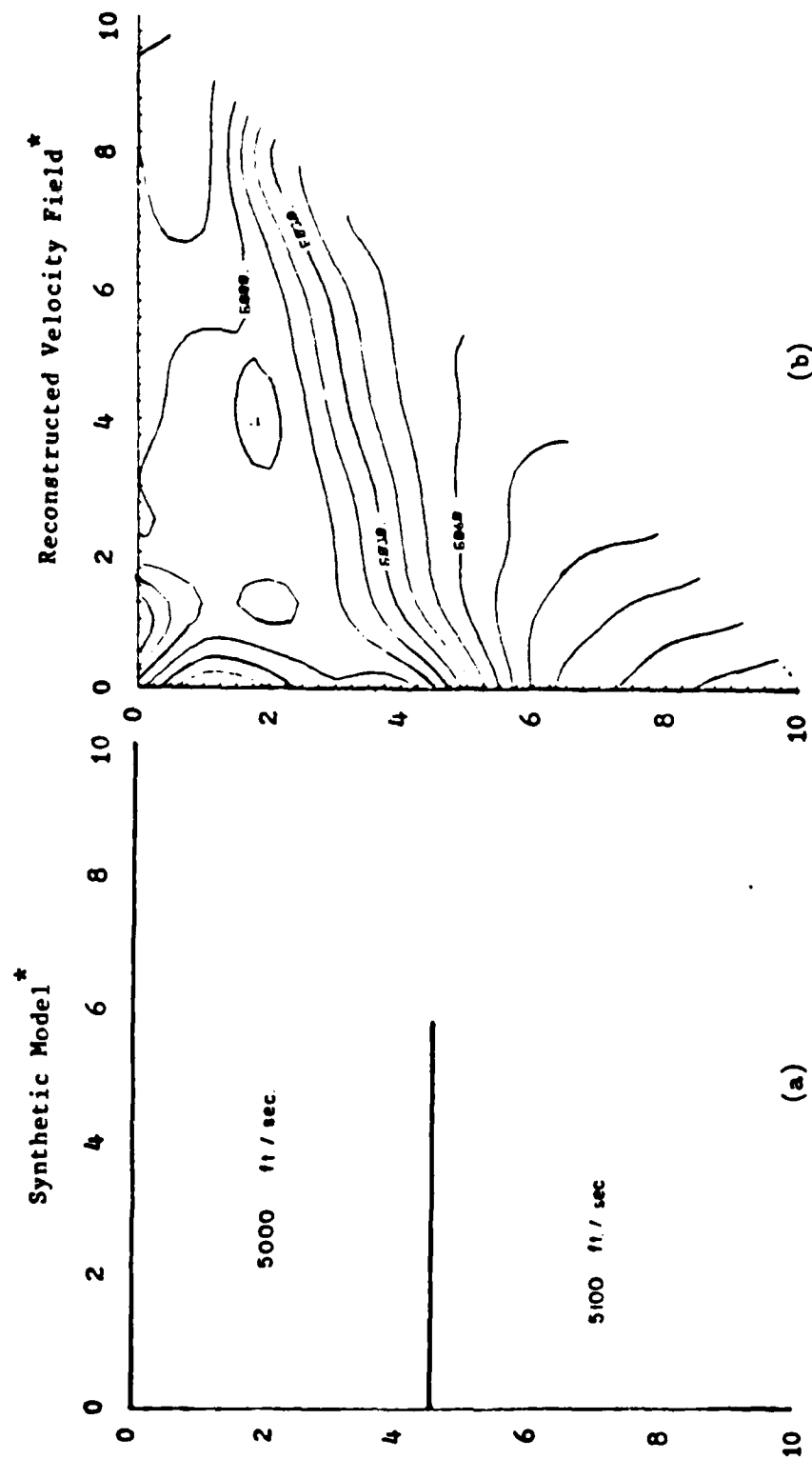


Figure 10. Velocity increasing with  $x$  and  $z$ .

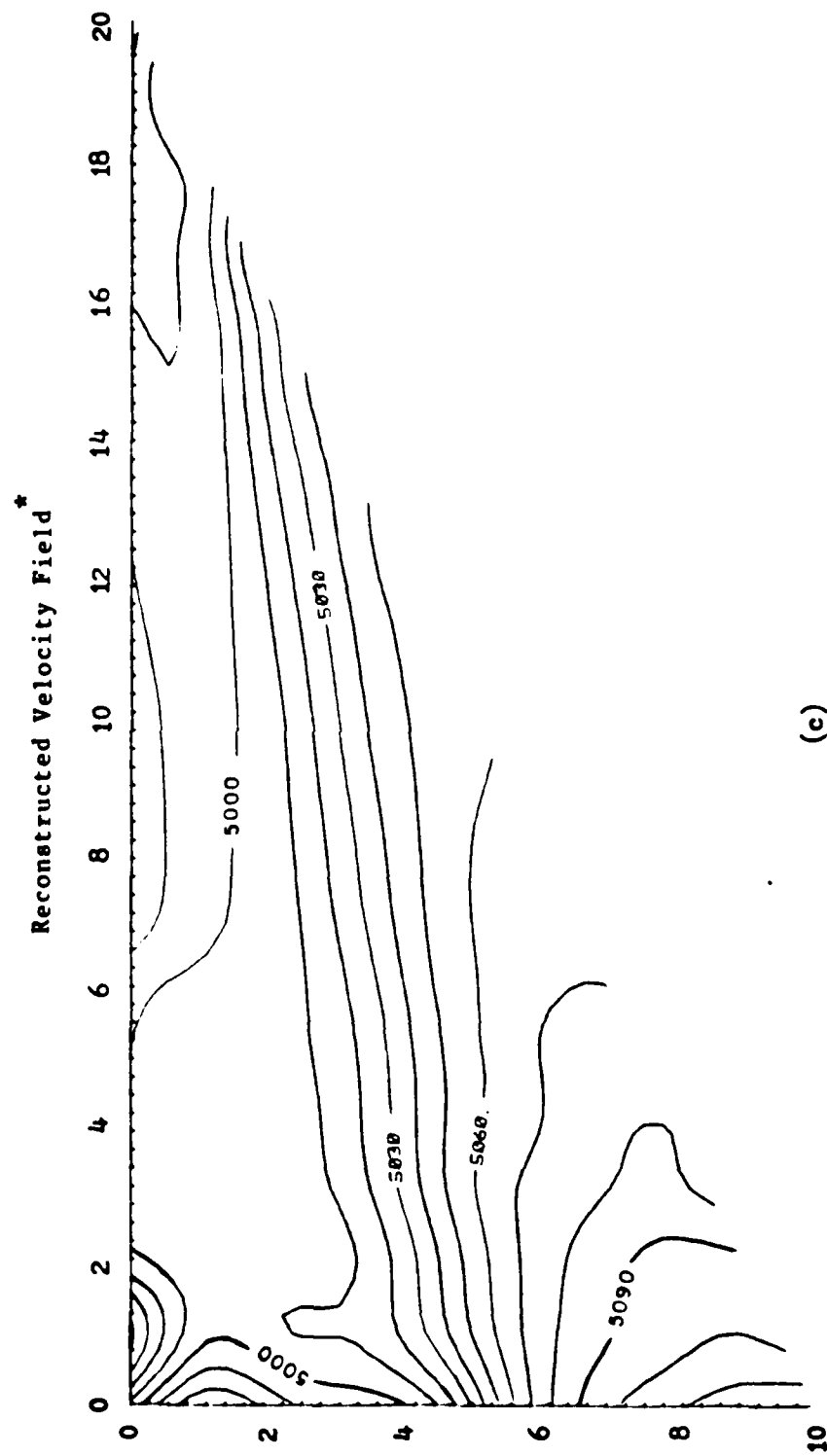
\*Travel times calculated using straight rays.

\*\* After 7 iterations using straight rays.



\* Travel times calculated using straight rays. \* After 13 iterations using straight rays.

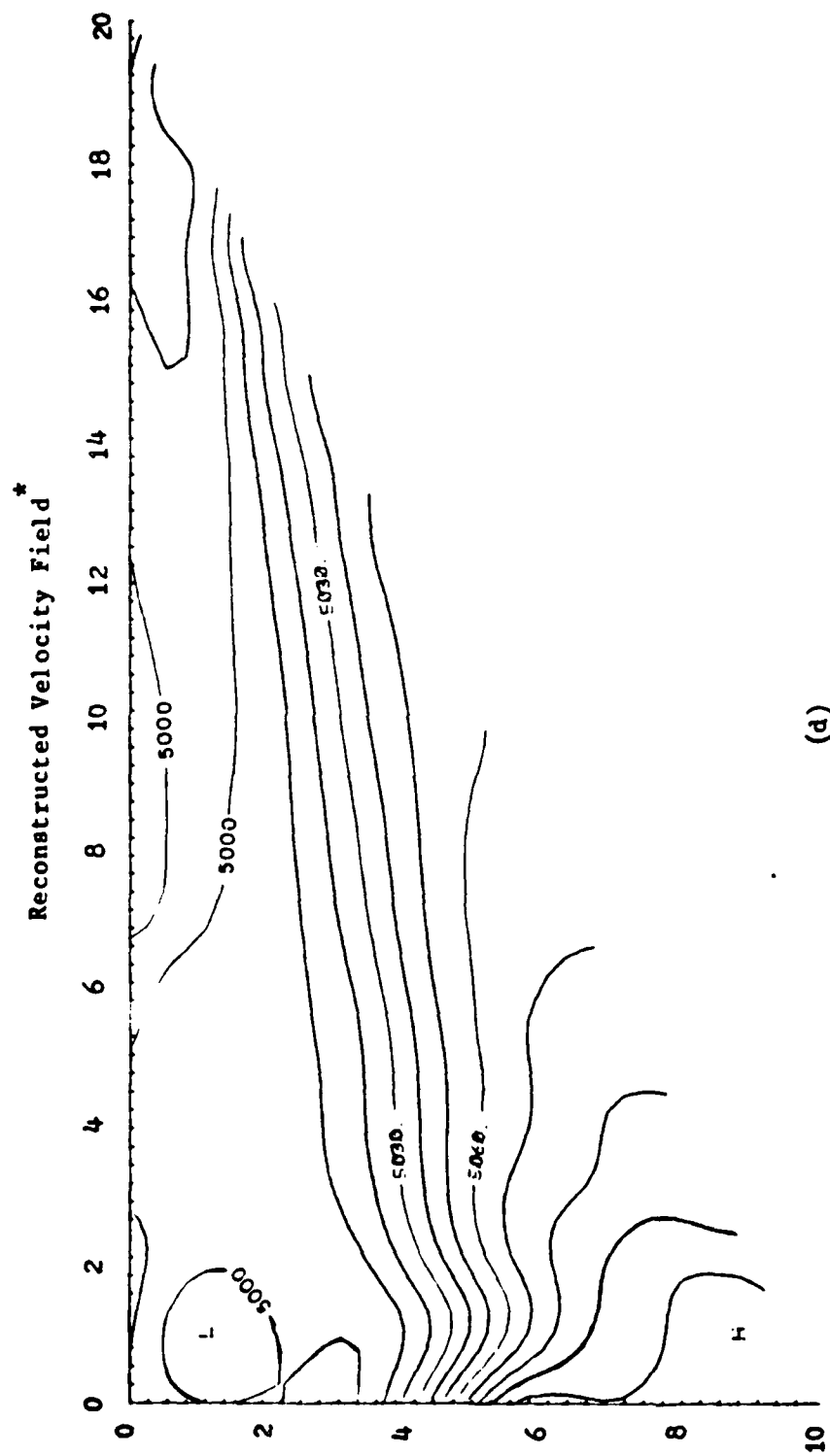
Figure 11. Two-layered model.



(c)

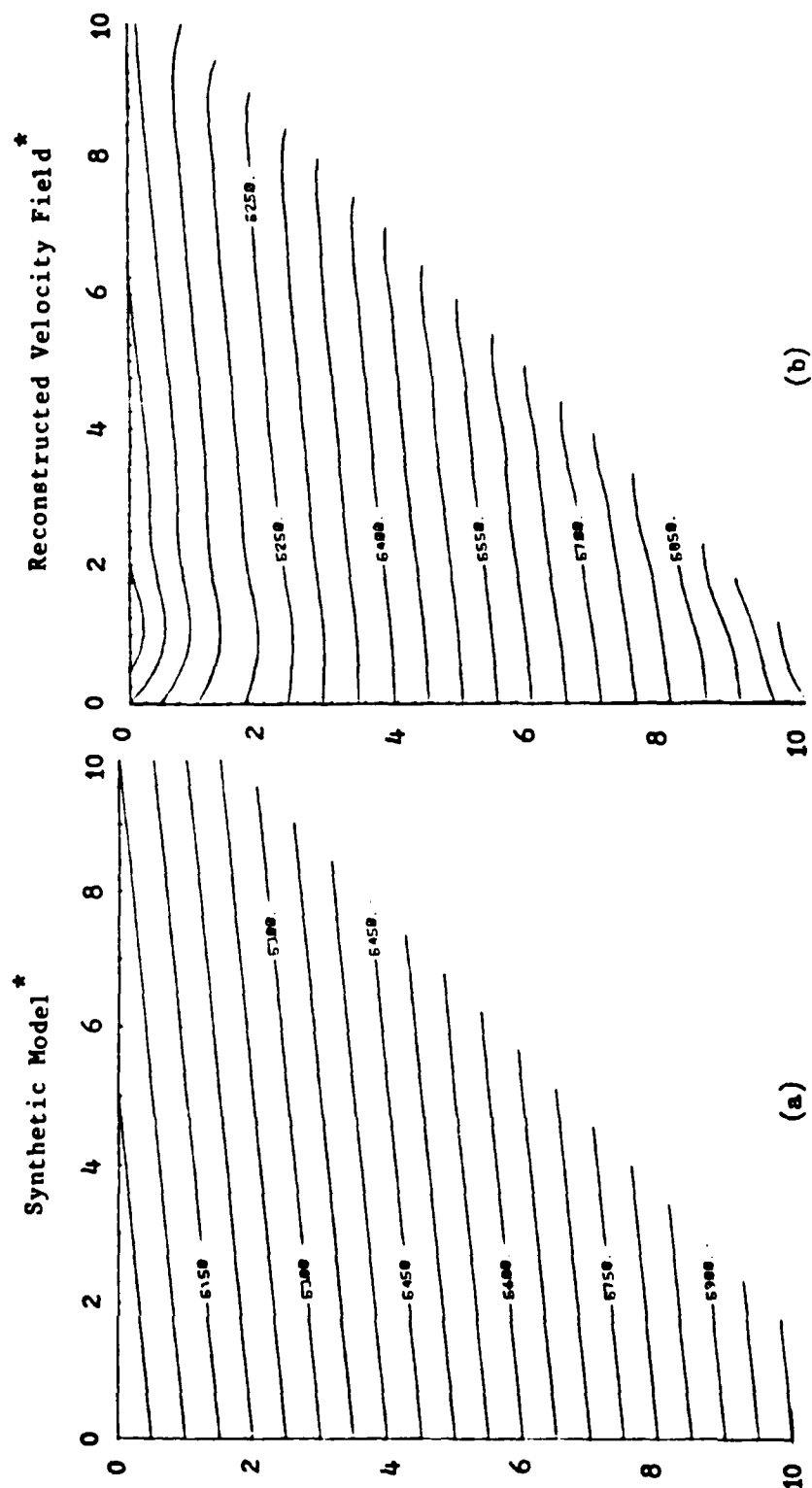
\* After 10 iterations using straight rays.

Figure 11. Two-layered model.



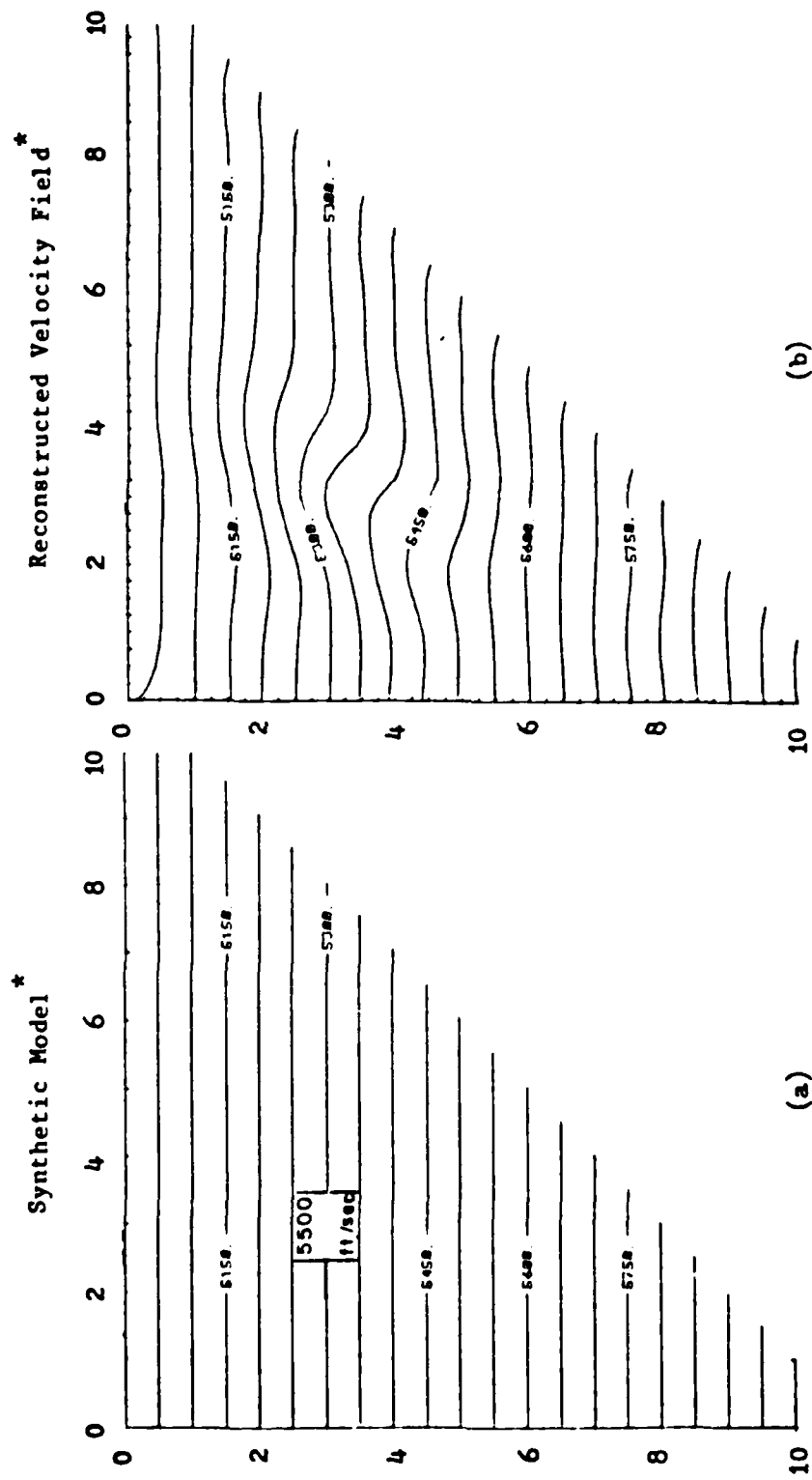
\* After 12 iterations using straight rays. Velocity parameters were constrained down the well (z-axis).

Figure 11. Two-layered model.



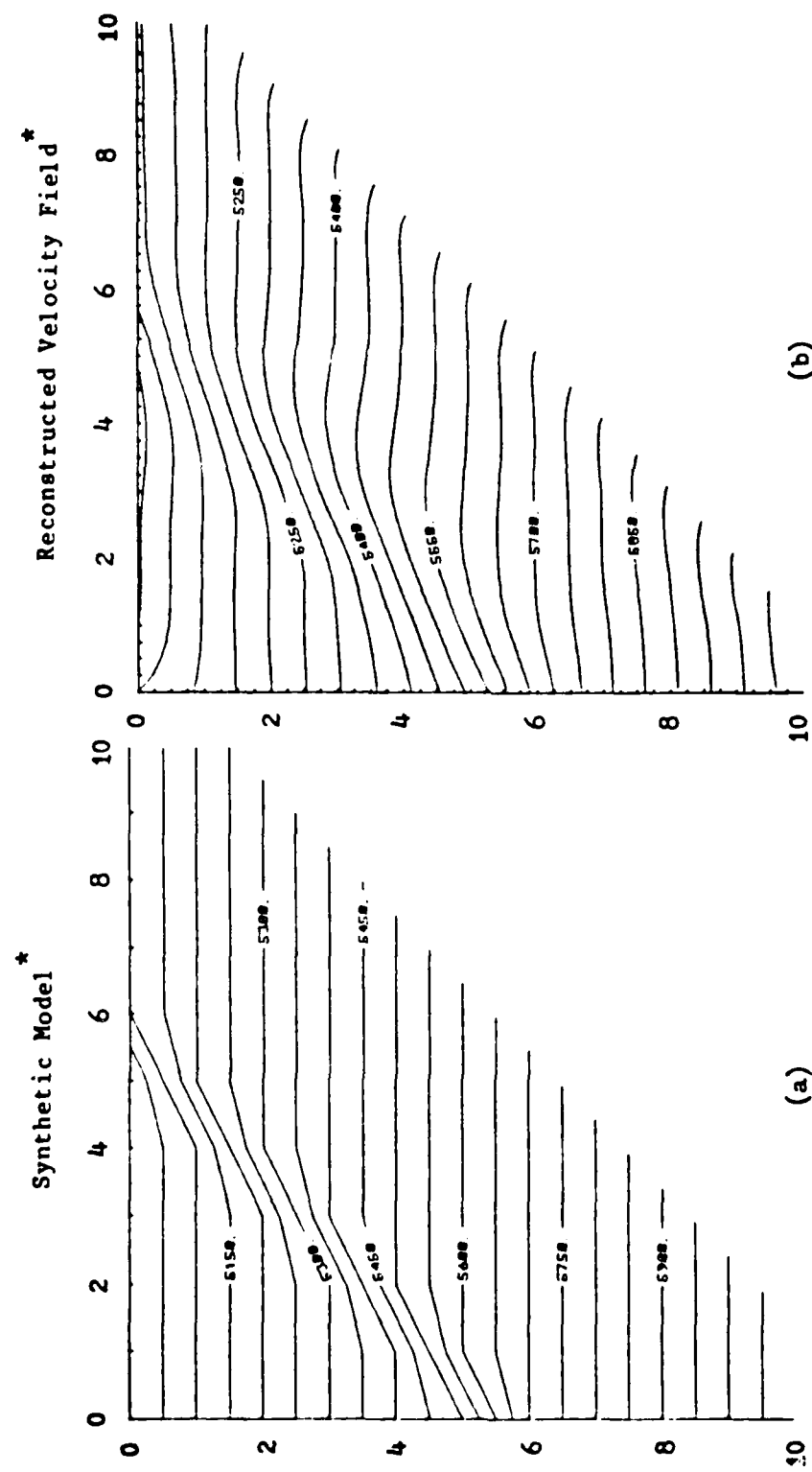
\* Travel times calculated using curved rays based on a background velocity  $-v(z) = 5000 + z_j$ .  
 \* After 10 iterations using curved rays.

Figure 12. Dipping model.



\* Travel times calculated using curved rays based on a background velocity -  $v(z) = 5000 + z_j$ .  
 \* After 10 iterations using curved rays.

Figure 13. High velocity anomaly within a linear trend.



\* Travel times calculated using curved rays based on a background velocity -  $v(z) = 5000 + z_j$  ft./sec.

Figure 14. Faulted model.



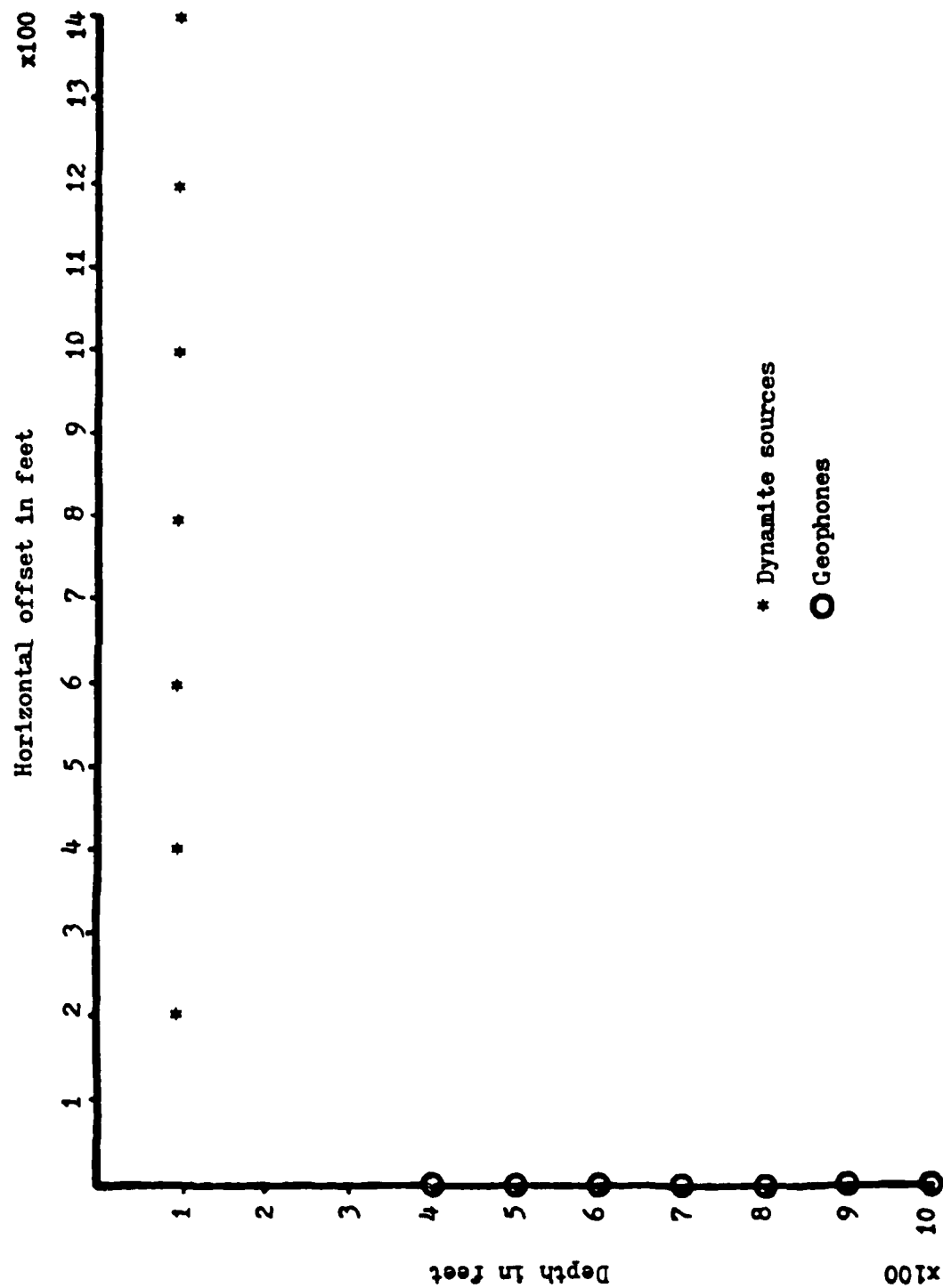
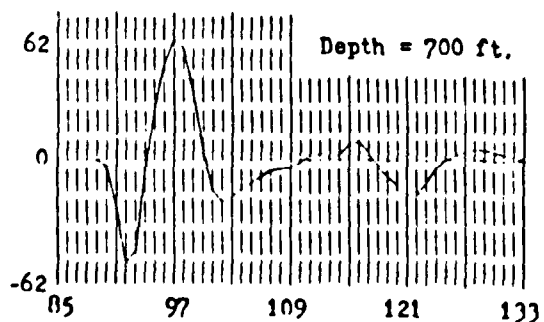
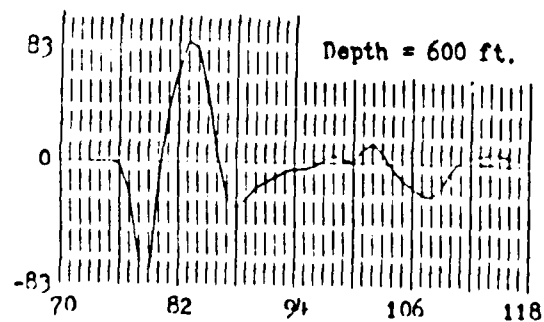
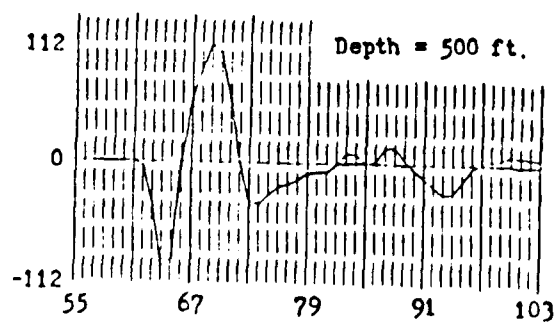
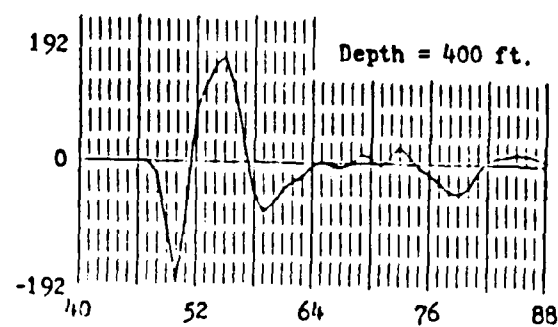


Figure 15. Field experiment layout.



Amplitude vs. Time (in ms.)  
for a source offset of 200 ft. and a  
receiver depth as shown.

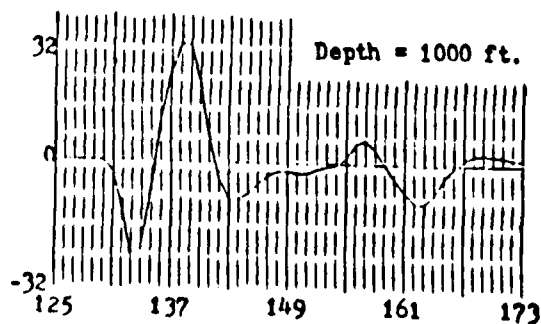
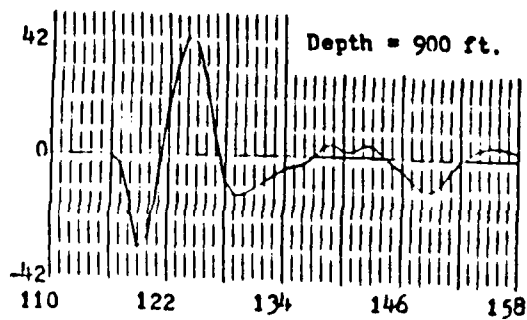
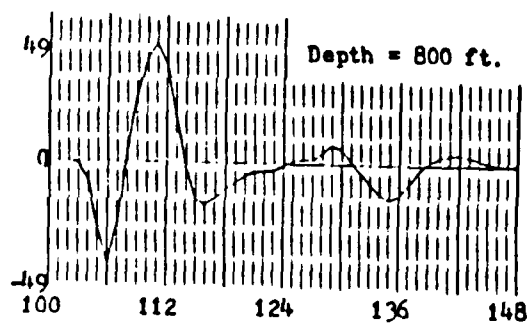
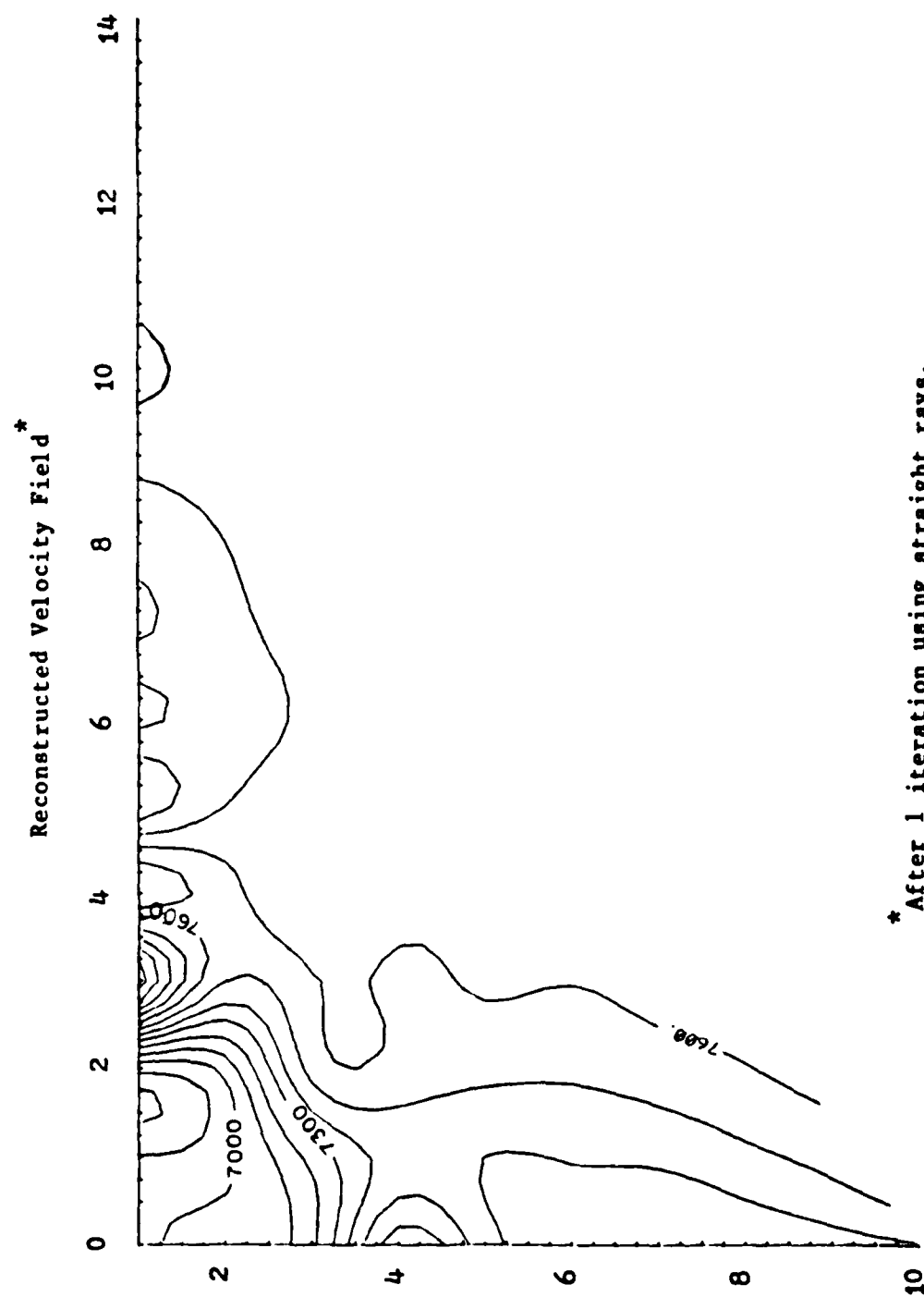
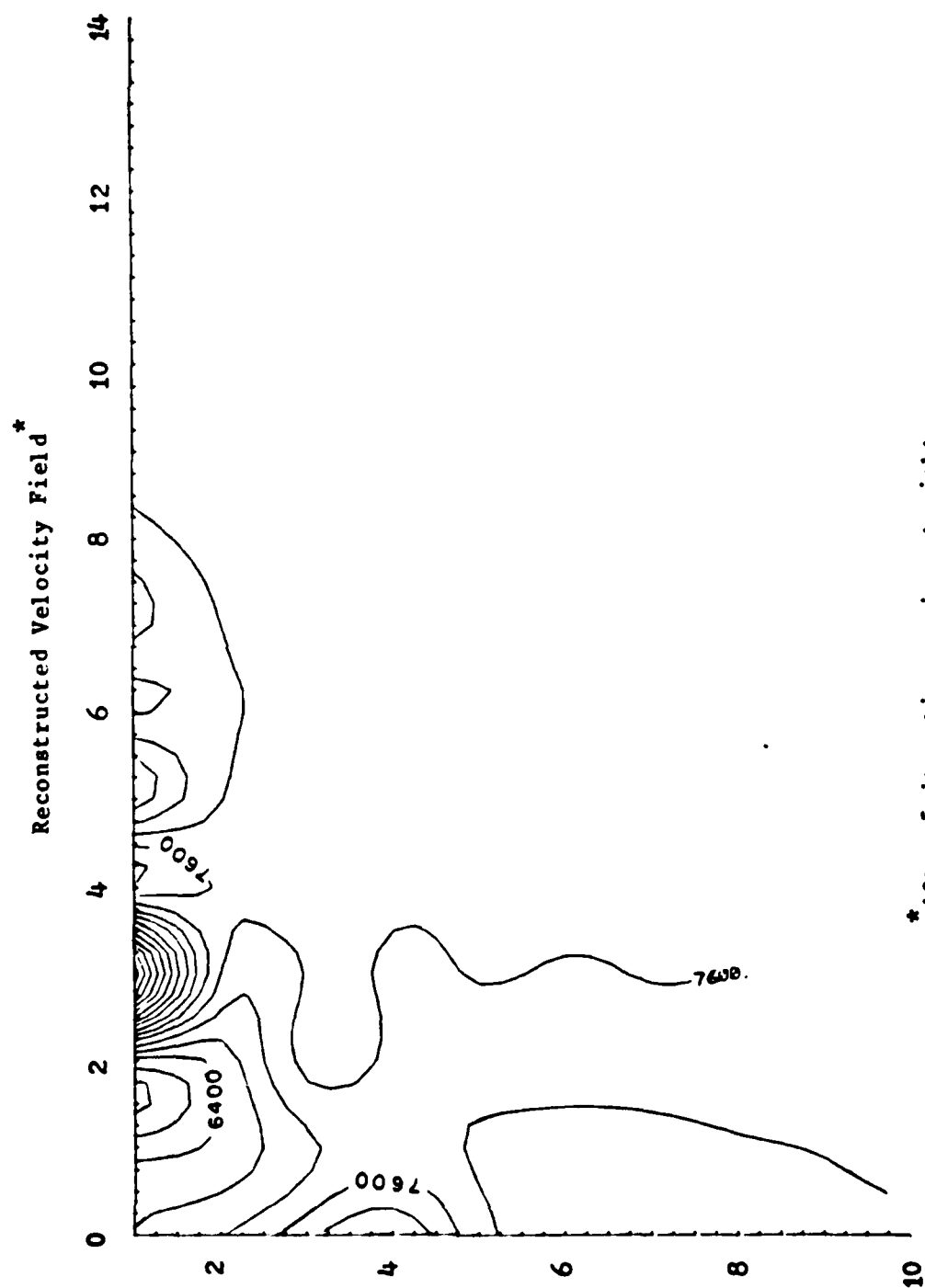


Figure 16. Typical waveforms.



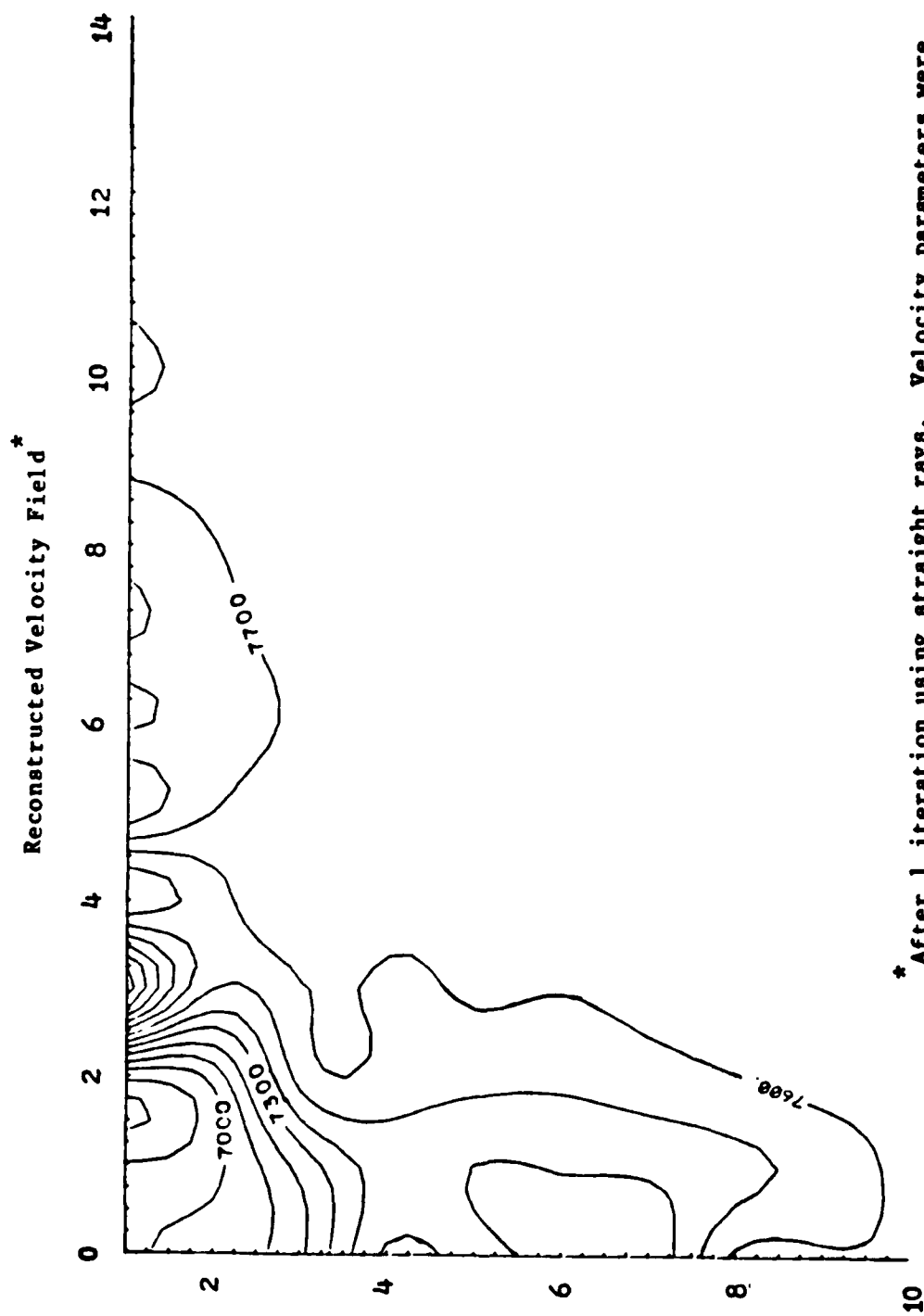
\* After 1 iteration using straight rays.

Figure 17a. Acoustic tomography from the Pierre Shale VSP data.



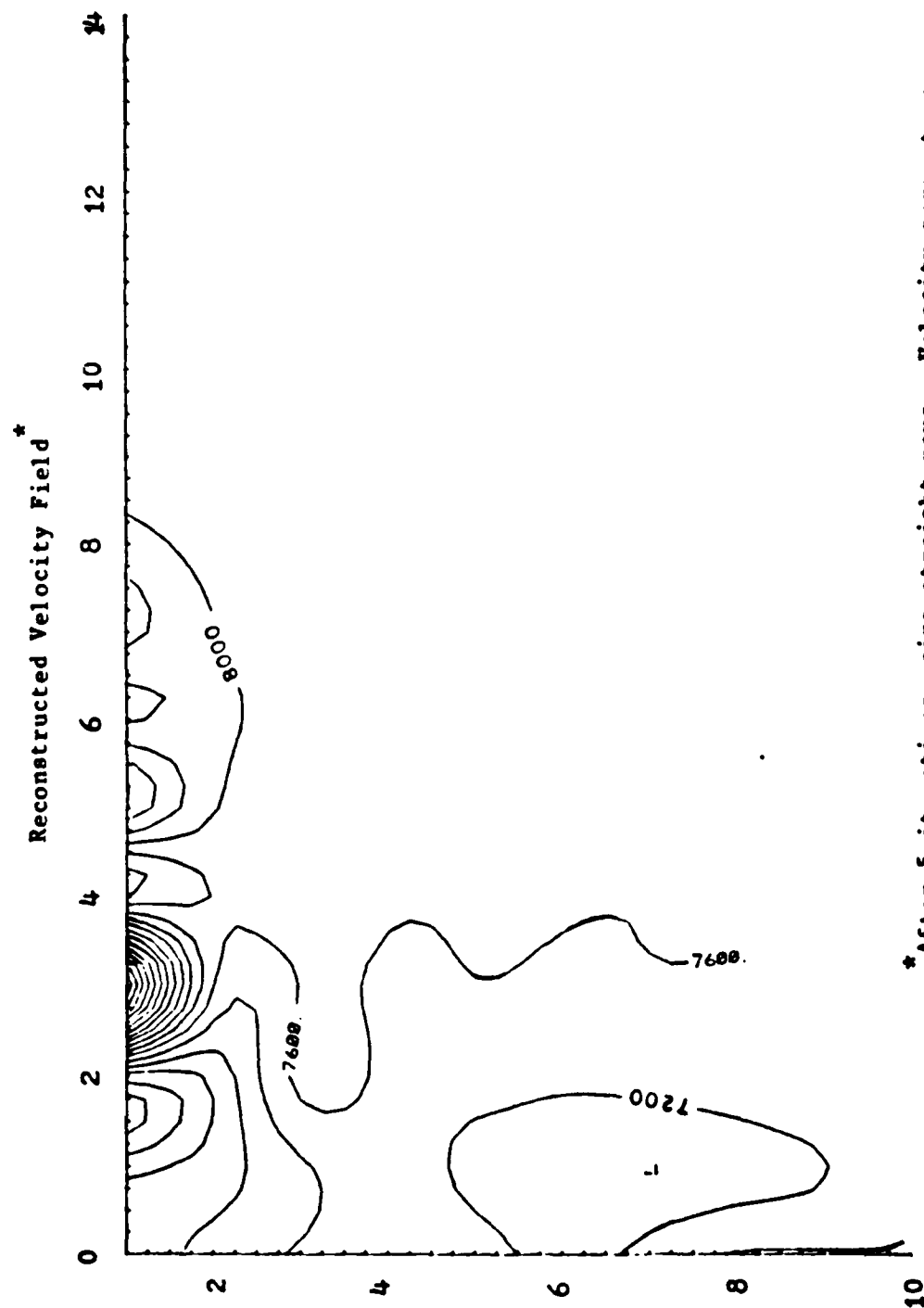
\* After 5 iterations using straight rays.

Figure 17b. Acoustic Tomography from the Pierre Shale VSP data.



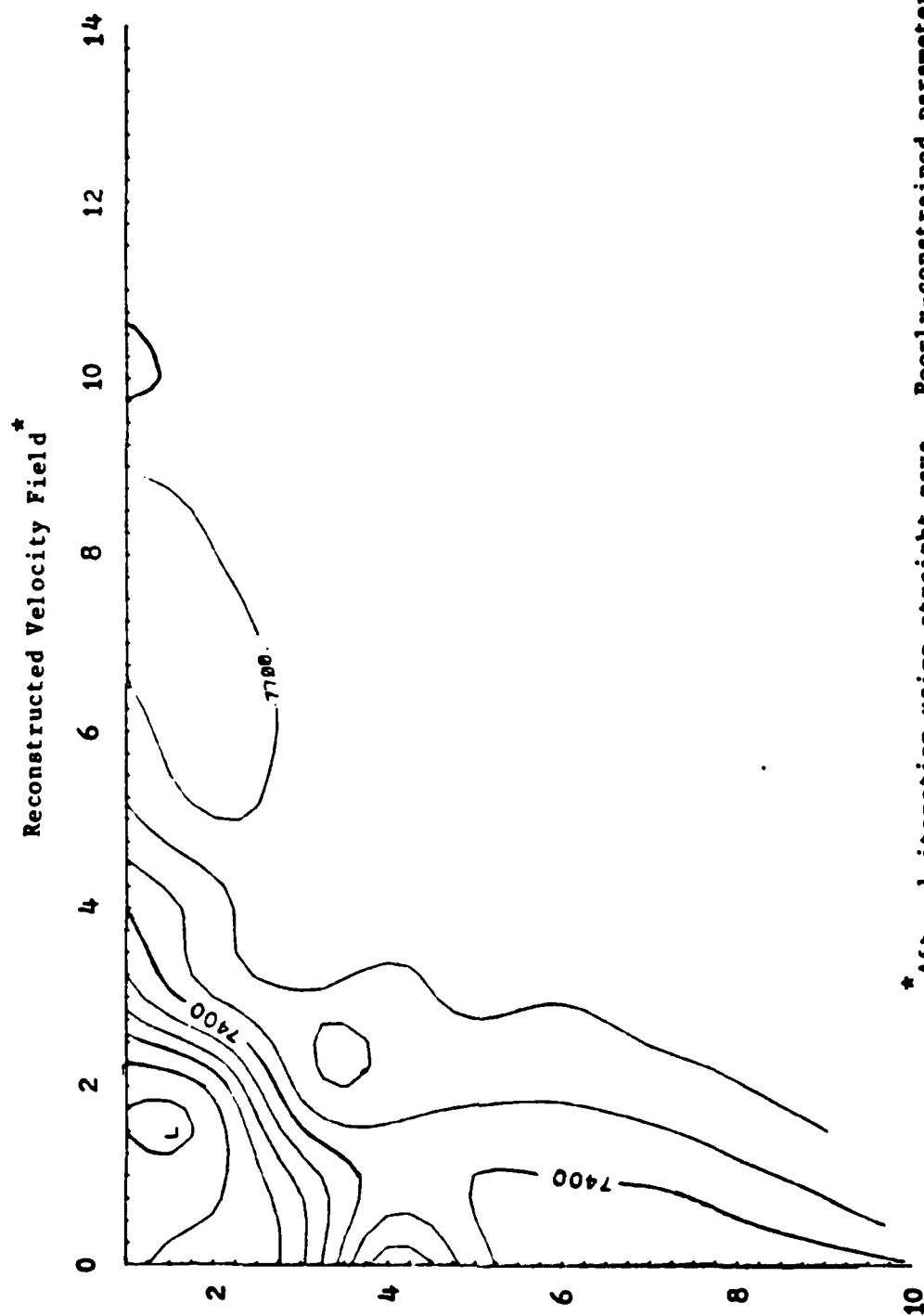
\* After 1 iteration using straight rays. Velocity parameters were constrained down the well (z-axis).

Figure 18a. Acoustic tomography from the Pierre Shale VSP data.



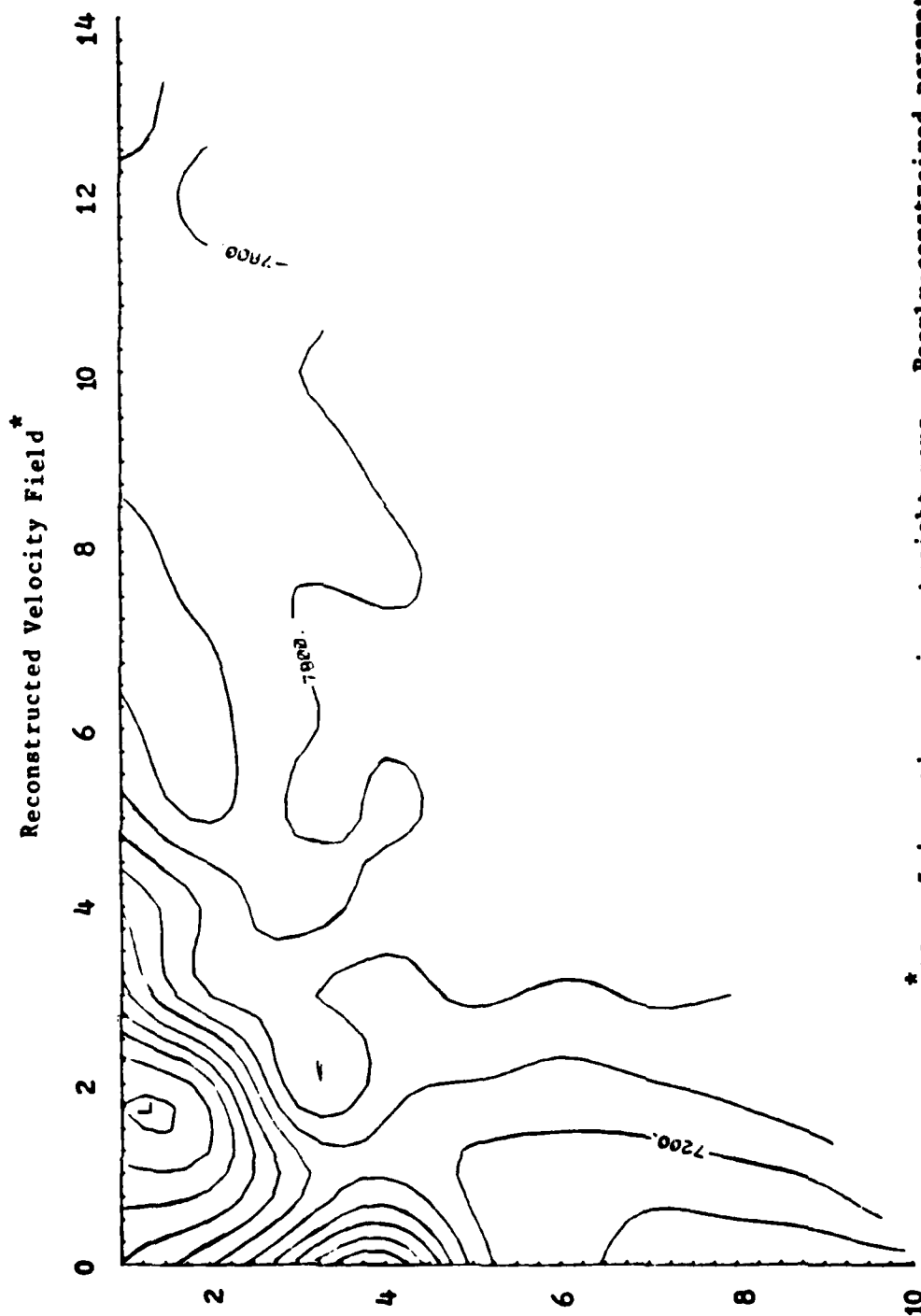
\* After 5 iterations using straight rays. Velocity parameters were constrained down the well (z-axis).

Figure 18b. Acoustic tomography from the Pierre Shale VSP data.



\* After 1 iteration using straight rays. Poorly-constrained parameters along the surface were eliminated from the image.

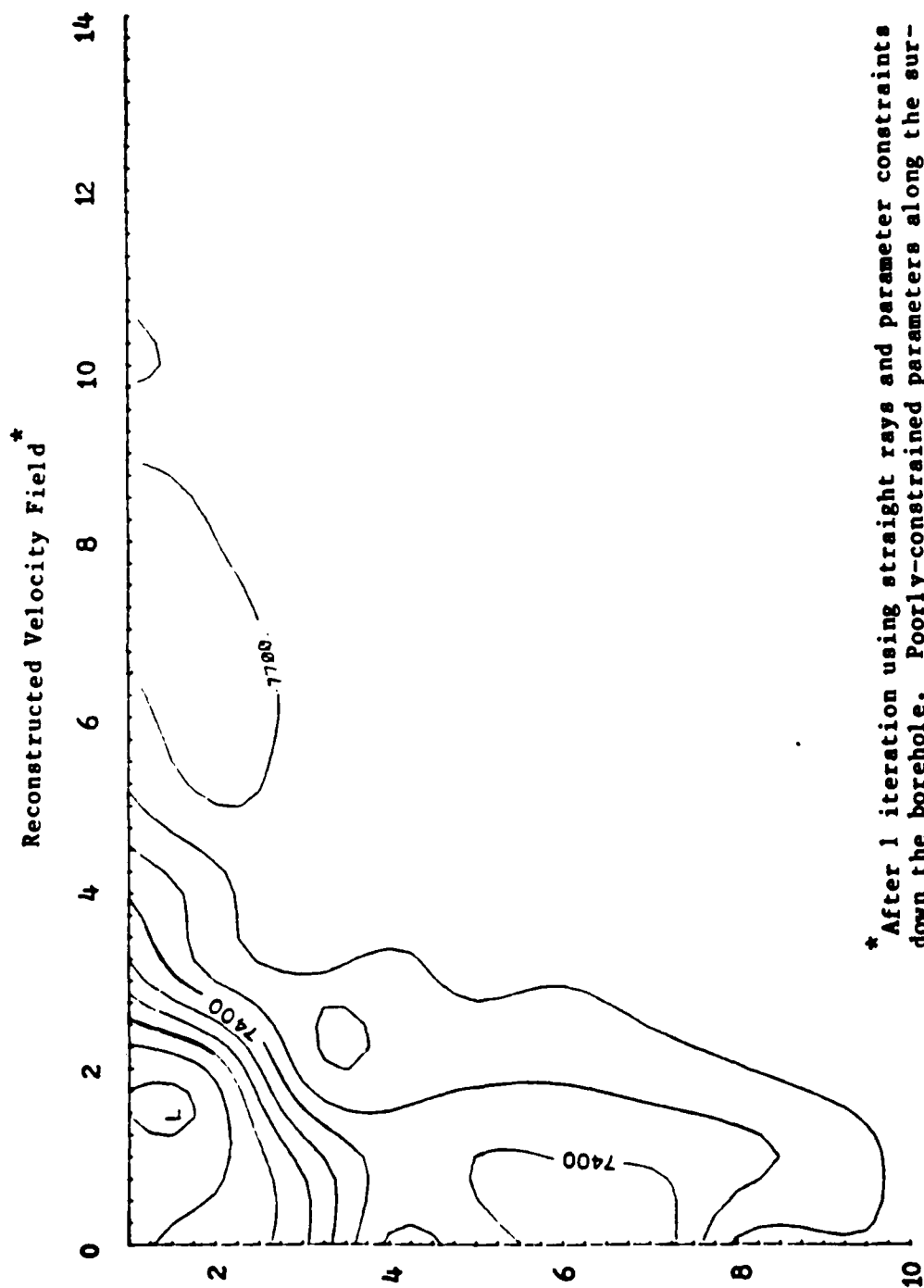
Figure 19a. Acoustic tomography from the Pierre Shale VSP data.



\*After 5 iterations using straight rays. Poorly-constrained parameters along the surface were eliminated from the image.

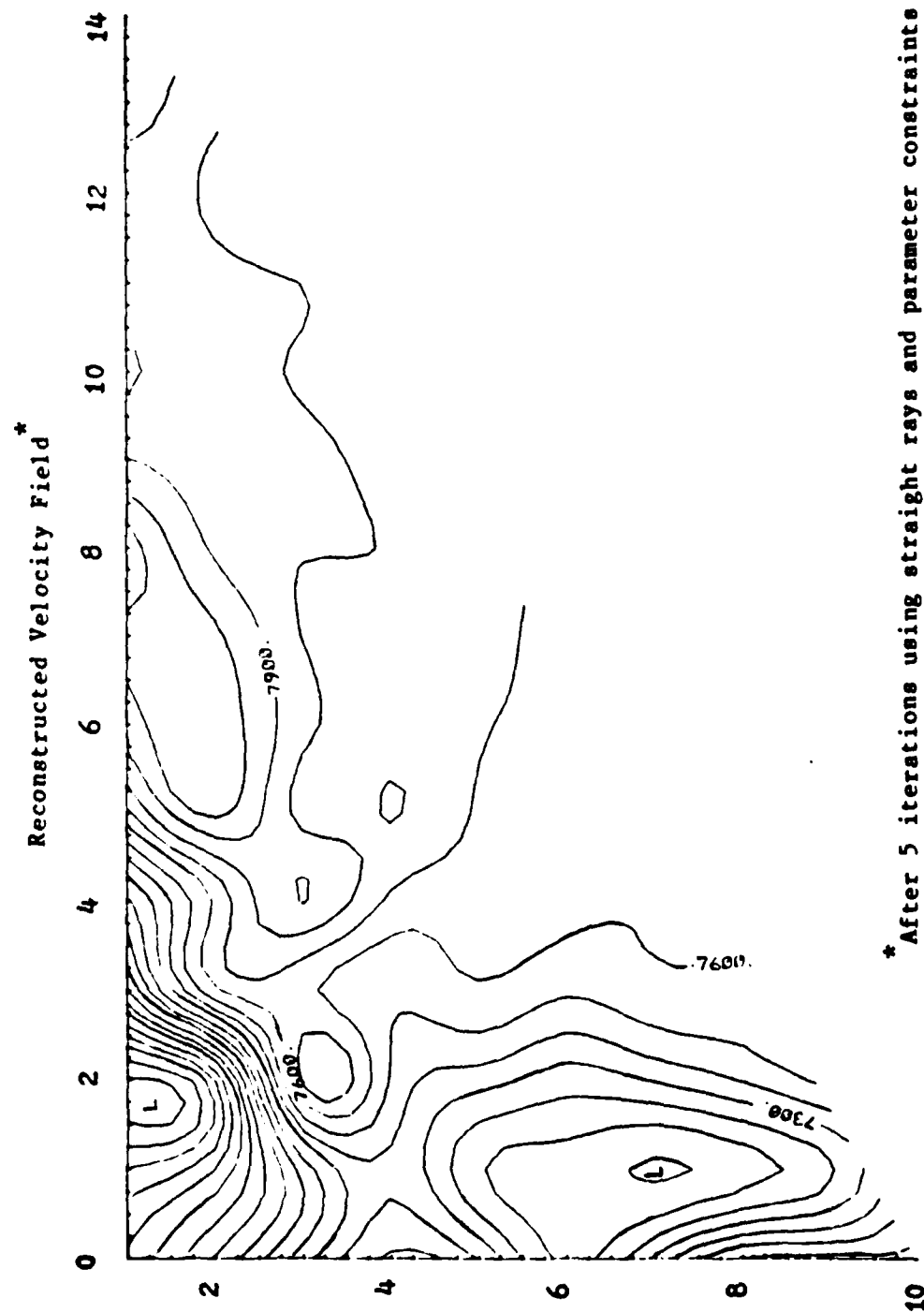
Figure 19b. Acoustic tomography from the Pierre Shale VSP data.





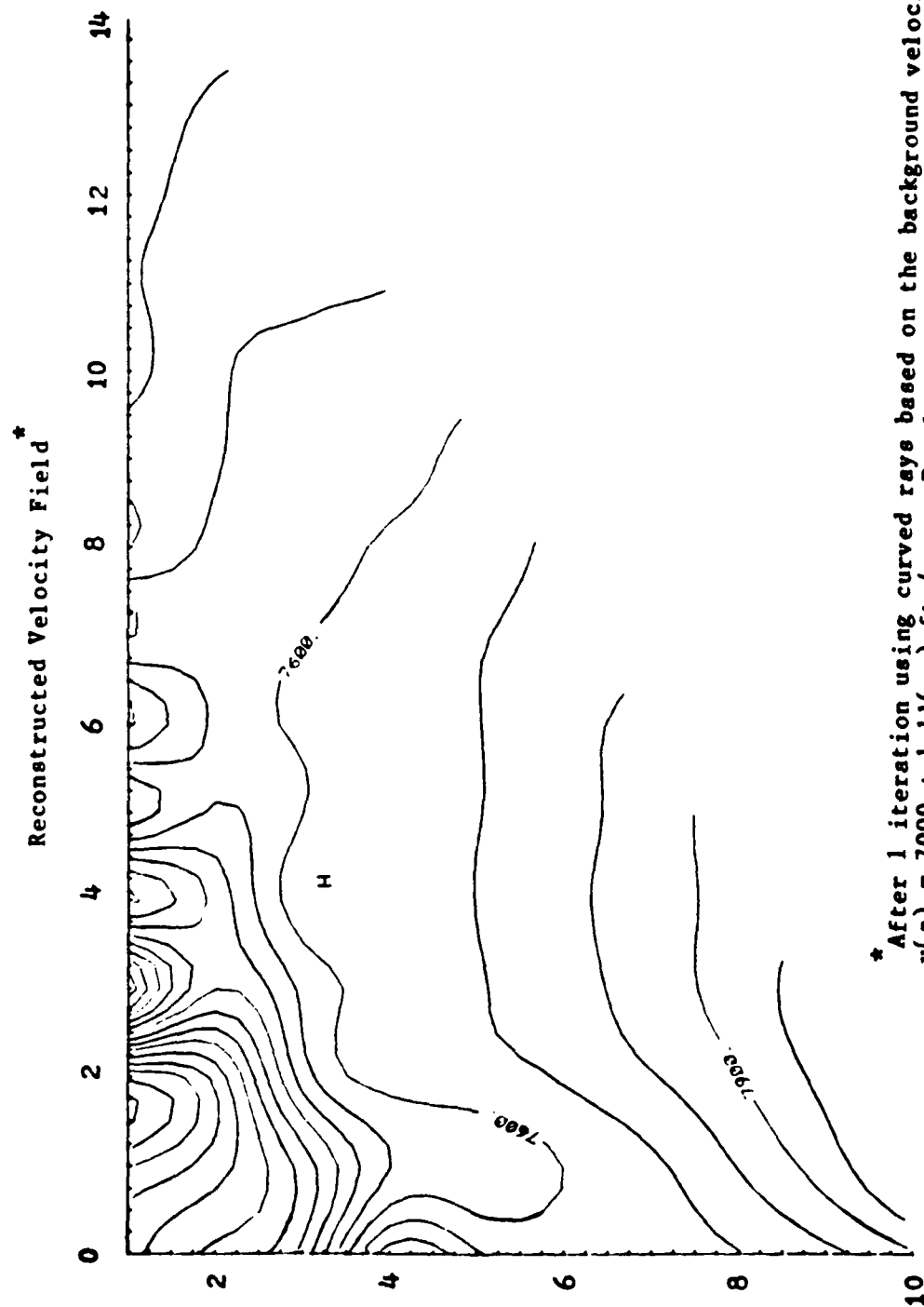
\* After 1 iteration using straight rays and parameter constraints down the borehole. Poorly-constrained parameters along the surface were eliminated from the image.

Figure 20a. Acoustic tomography from the Pierre Shale VSP data.



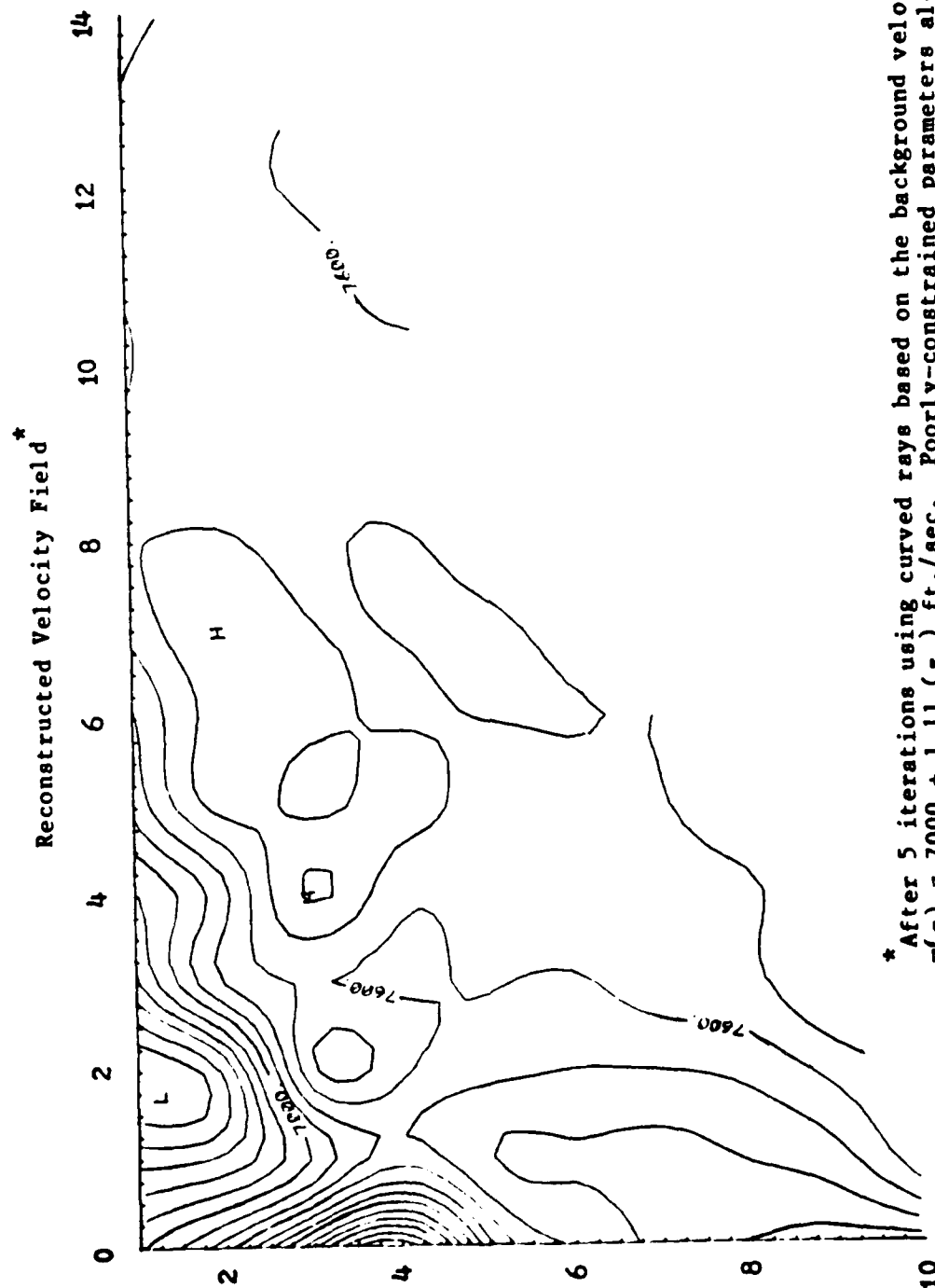
\* After 5 iterations using straight rays and parameter constraints down the borehole. Poorly-constrained parameters along the surface face were eliminated from the image.

Figure 20b. Acoustic tomography from the Pierre Shale VSP data.



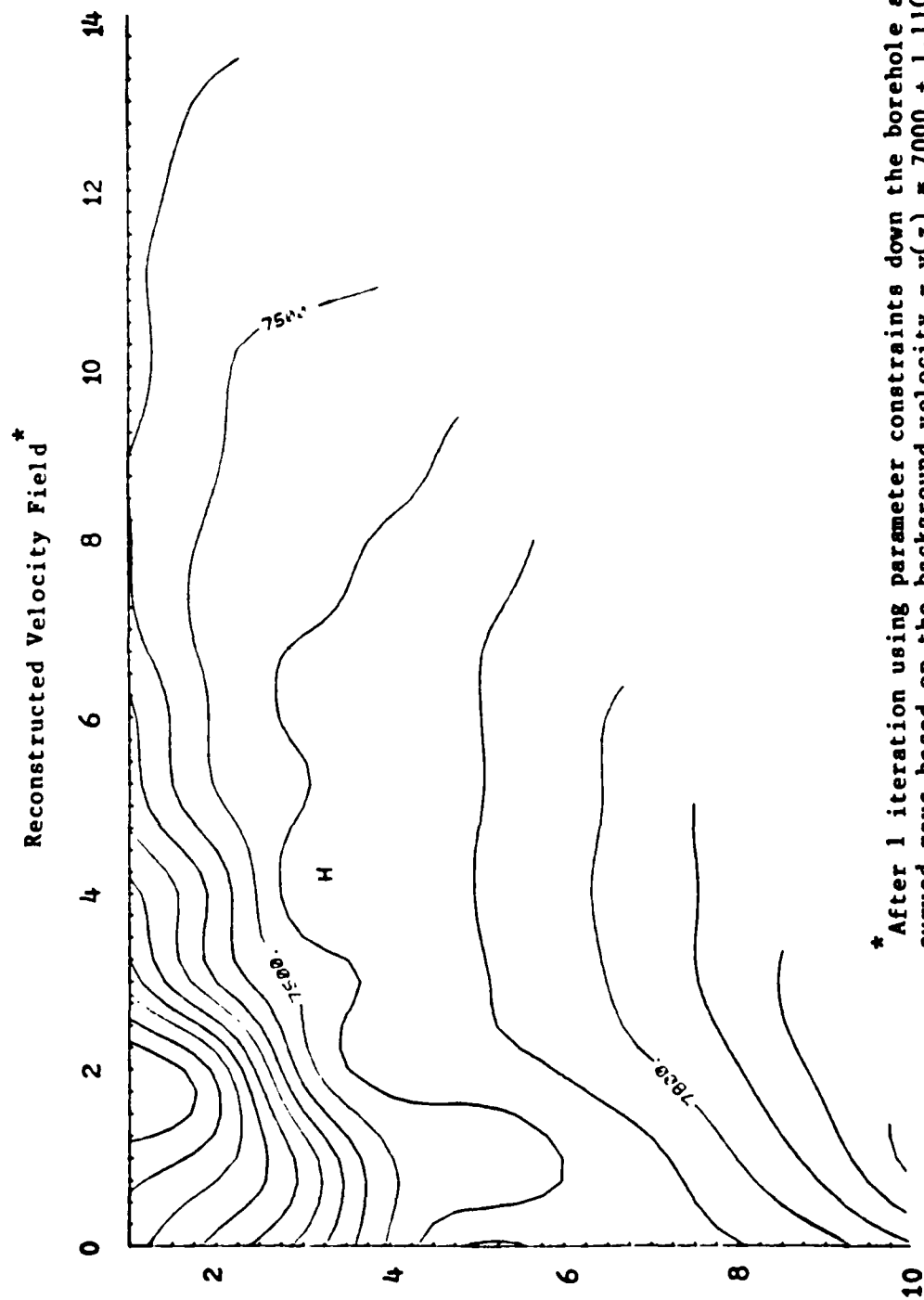
\* After 1 iteration using curved rays based on the background velocity -  $v(z) = 7000 + 1.11(z)$  ft./sec. Poorly-constrained parameters along the surface were eliminated from the image.

Figure 21a. Acoustic tomography from the Pierre Shale VSP data.



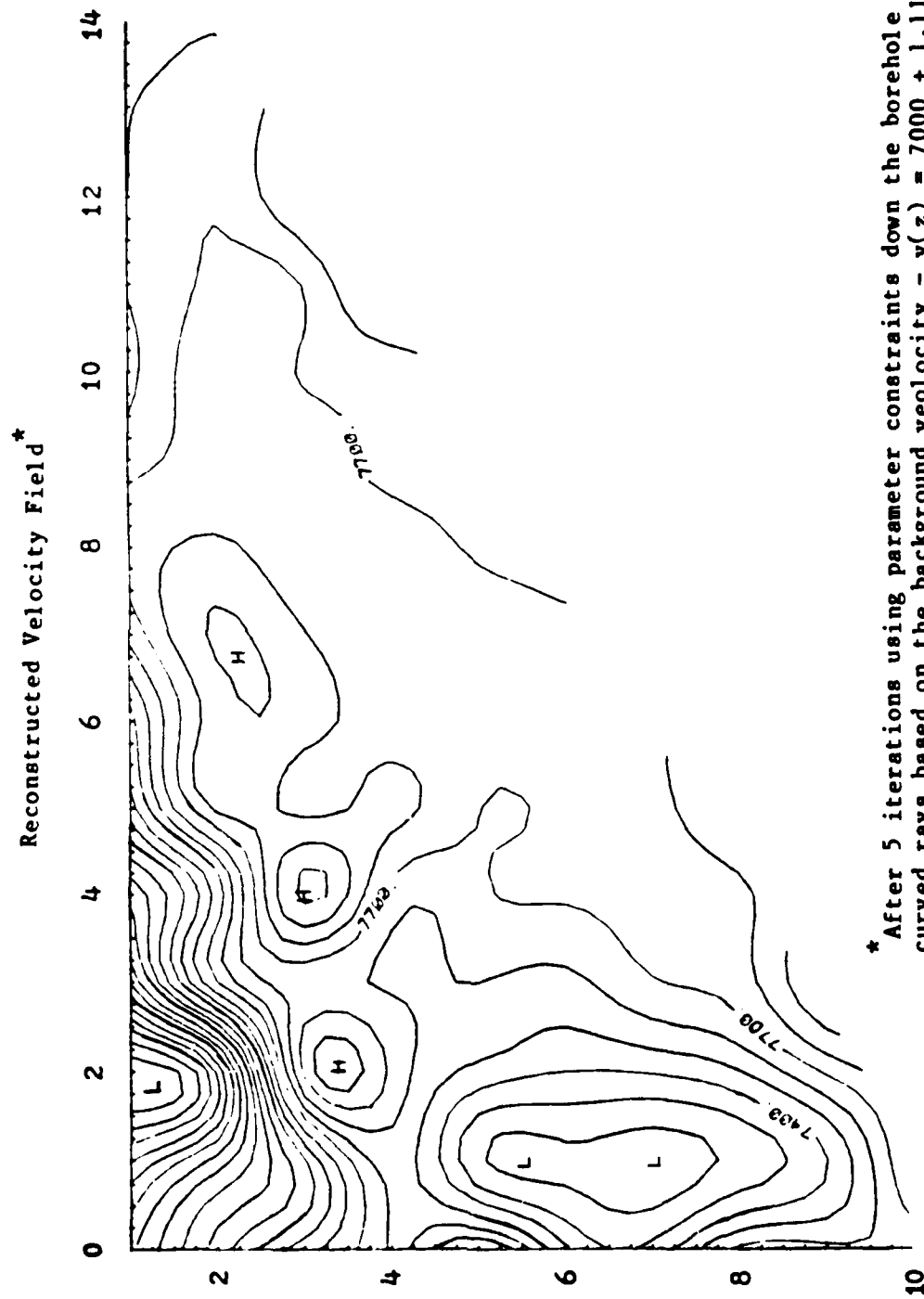
\* After 5 iterations using curved rays based on the background velocity -  $v(z) = 7000 + 1.11(z_i)$  ft./sec. Poorly-constrained parameters along the surface were eliminated from the image.

Figure 21b. Acoustic tomography from the Pierre Shale VSP data.



\* After 1 iteration using parameter constraints down the borehole and curved rays based on the background velocity  $-v(z) = 7000 + 1.11(z)$  ft./sec. Poorly-constrained parameters along the surface were eliminated from the image.

Figure 22a. Acoustic tomography from the Pierre Shale VSP data.



\* After 5 iterations using parameter constraints down the borehole and curved rays based on the background velocity  $-v(z) = 7000 + 1.11(z)$  ft./sec. Poorly-constrained parameters along the surface were eliminated from the image.

Figure 22b. Acoustic tomography from the Pierre Shale VSP data.

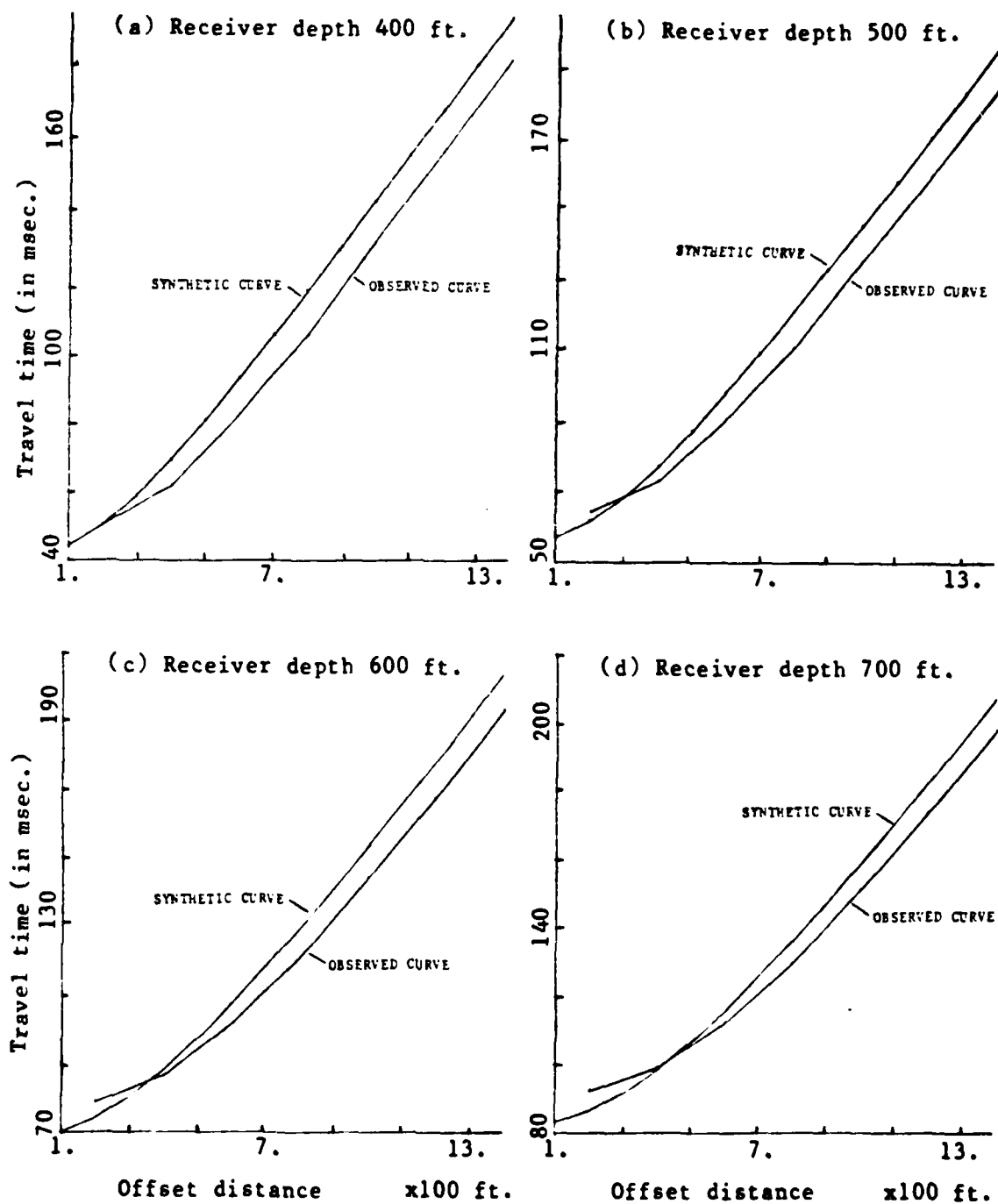


Figure 23. Travel time curves.

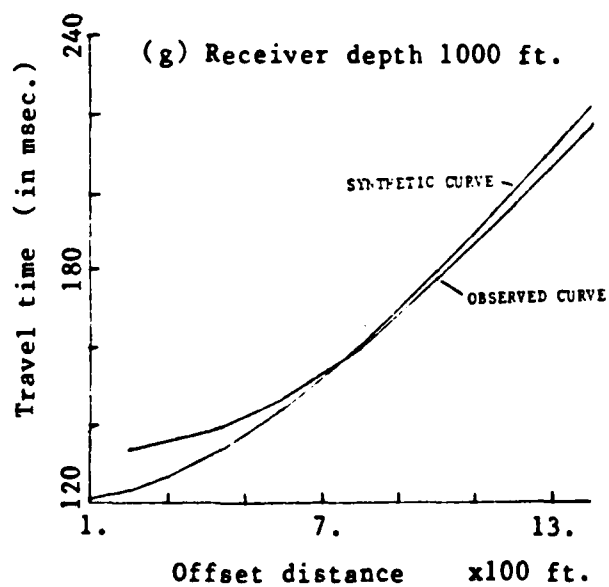
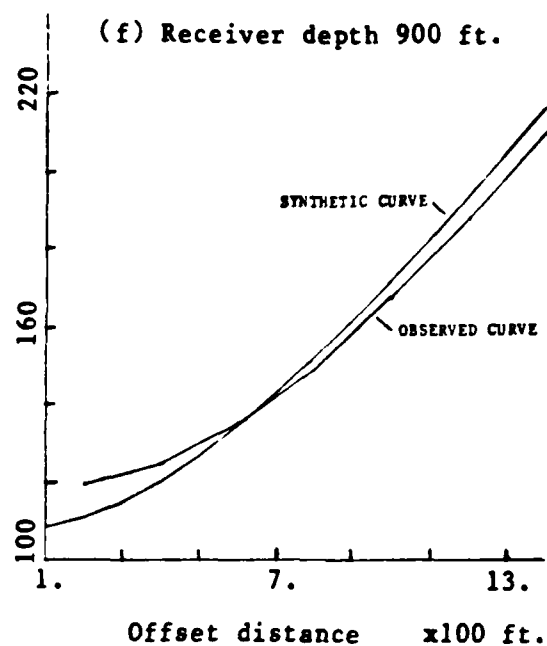
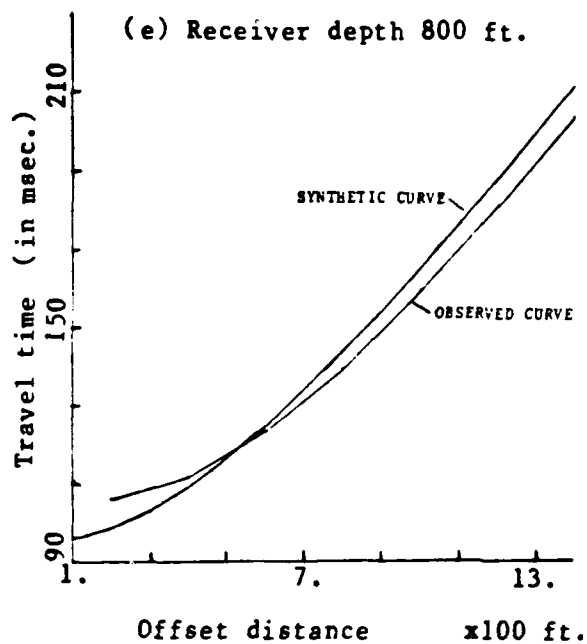


Figure 23. Travel time curves.



ABSTRACT

An algebraic reconstruction technique (ART) is described for the seismic tomography of velocities from the travel times of a multiple offset vertical seismic profile. ART concentrates on the production of a reconstructed field whose projected data (travel times) agree with the observed data. This reconstructed field is modified by altering the data for each ray such that when this data is back-projected, the new image agrees with the original data. Because the paths of the rays must be known to calculate the expected travel times, the problem is linearized by using raypath approximations as determined from either a constant or a linear  $c(z)$  velocity medium.

Imaging of synthetic data revealed that the orientation of the anomaly affects both the rate of convergence and the resolution of the reconstructed field. Some smoothing of the velocity anomalies occurred along the direction of the rays.

Noisy data sets developed problems in the reconstructed velocity field. Huge single point anomalies appeared along the model's edge in the reconstructed image. Elimination of these errant anomalies was necessary to obtain a reasonable velocity reconstruction. Because isotropy was assumed, the algorithm poorly reconstructed data which was collected over the strongly anisotropic Pierre Shale.

**END**

**FILMED**

1-85

**DTIC**